ANALYSIS AND DEMONSTRATION: A PROOF-OF-CONCEPT COMPASS STAR TRACKER

A Thesis

by

MICHAEL JOHN SWANZY

Submitted to the Office of Graduate Studies of
Texas A&M University
in partial fulfillment of the requirements for the degree of

MASTER OF SCIENCE

December 2005

Major Subject: Aerospace Engineering

ANALYSIS AND DEMONSTRATION: A PROOF-OF-CONCEPT COMPASS STAR TRACKER

A Thesis

by

MICHAEL JOHN SWANZY

Submitted to the Office of Graduate Studies of
Texas A&M University
in partial fulfillment of the requirements for the degree of

MASTER OF SCIENCE

Approved by:

Chair of Committee,	John E. Hurtado
Committee Members,	John L. Junkins
	Daniele Mortari
	Shankar P. Bhattacharyya
Head of Department,	Helen L. Reed

December 2005

Major Subject: Aerospace Engineering

ABSTRACT

Analysis and Demonstration: A Proof-of-Concept Compass Star Tracker. (December 2005)

Michael John Swanzy, B.S., Texas A&M University

Chair of Advisory Committee: Dr. John Hurtado

This research analyzes and demonstrates the local position determination problem on Earth using a novel instrument, the Compass Star Tracker. Special focus is given to the theoretical development of the mathematics of local position determination, the design and fabrication of a proof-of-concept instrument, an error source analysis, and the experimental tests used to validate the position determination concepts.

Star sensors are typically used as attitude determination instruments on spacecraft orbiting Earth. In this capacity, the star sensor determines the orientation of the spacecraft using digital images of the stars. This research utilizes the basic functionality of the star sensor in a new way; the orientation information from the star image is used to determine a user's latitude and longitude coordinates on Earth. This concept is valuable because it allows users to determine their position autonomously.

The fundamental concepts that enable local position determination were originally published in Drs. Samaan, Mortari, and Junkins (AAS 04-007). This research improves upon that work by eliminating the zenith-orientation constraint and providing several crucial theoretical corrections. In addition to the position determination mathematics, this research provides analysis of the theoretical and practical error sources associated with the position determination problem. This research also details the design, fabrication, and experimental test program of a proof-of-concept

Compass Star Tracker. Together, the theoretical development, error analysis, instrument design, and test program serve as validation of the the position determination concept. This work is intended as the first of many steps toward eventual deployment of autonomous position determination sensors on the Moon and Mars.

To my parents

ACKNOWLEDGMENTS

Special thanks to Dr. John Hurtado for his guidance, support, encouragement, and the countless opportunities he afforded me. I will always remember that my success in this graduate program is owed in large part to him. Many thanks also to Dr. Daniele Mortari and Dr. John Junkins for their patient tutorials, acute reflections, and their service on my graduate committee.

This research effort was sponsored in its entirety by Dr. David Boyle and Mr. Nick Combs of the Spacecraft Technology Center. Thanks to Dr. Boyle and Mr. Combs for their belief in this project. Additional thanks to the entire STC professional staff for their assistance, specifically Steven Summers, Partrick Marquardt, Steven Eskridge, Joe Perez, and Malak Samaan. Without their extensive contributions and generous technical advice, the proof-of-concept instrument would not have been built.

Use of the Rojo Grande Ranch was made possible by the generosity of the Schoessow family, and for that I am grateful. Thanks also to the Bonn's for allowing me to work on their ranch during the earliest stages of this project. I would be remiss to omit thanks to all of the people who have given me the encouragement and support I needed to complete this project. My sincere thanks to Kate, my parents, my sisters, and my friends.

It is humbling to find oneself seated unexpectedly at the intersection of Science and Beauty, and I know my time there was a fleeting gift that I will always cherish. For cold and dark mornings beneath millions of stars, I thank God.

TABLE OF CONTENTS

CHAPTER Page

Page

LIST OF TABLES

LIST OF FIGURES

FIGURE Page

CHAPTER I

INTRODUCTION

For thousands of years, one of mankind's most enduring scientific challenges has been finding an accurate and reliable means of navigating the Earth. This quest spurred the invention of instruments such as the sextant and revolutionary advances in the accuracy of chronometers. Today, the Global Positioning System (GPS) represents the state of the art navigational tool. The GPS is a network of satellites and ground stations that benefit military and civilian users worldwide. The high-frequency radio waves generated by the GPS satellites transmit the necessary data for a user, with a GPS receiver, to precisely determine his latitude and longitude position on Earth as well as bearing, elevation, and rate of travel.

An alternative to the traditional, GPS-like signal triangulation method for position determination exists in the proposed Compass Star Tracker (CST)[1]. The CST concept is actually a modern day improvement on the navigational techniques that explorers have used for thousands of years. Put simply, the CST will determine local position by taking and analyzing a picture of the stars in the night sky. The Compass Star Tracker will utilize digital star imaging, star identification, terrestrial orientation parameters, and attitude determination to autonomously determine the user's latitude, longitude, and bearing on a given terrestrial body. With this approach, the stars on the celestial sphere assume the role of the satellites in the GPS-model. The ability to autonomously establish local latitude and longitude information thereby eliminates the need for expensive satellite constellations. For this reason and others,

---

The journal model is the *Journal of Guidance, Control and Dynamics.*

the CST is an excellent candidate for local position determination on the Moon and Mars. Although the benefits of the GPS currently outweigh those of the CST for use on Earth, the successful demonstration of the CST concepts on Earth will pave the way for potential CST deployment on the Moon and Mars. The fundamental concepts that make local position determination possible are attitude determination, digital star imaging, star identification, and incorporation of the terrestrial orientation parameters. These topics, as well as the thesis objectives, will now be introduced.

A. Attitude Determination

Attitude determination is the process of calculating the relative orientation between two coordinate reference frames in space. The classic attitude determination problem requires two corresponding sets of vector observations; one set for each of the two reference frames being considered. If the vector observations are the product of sensor measurements, there will invariably be some amount of error associated with each vector. Due to these errors, the attitude determination process outputs an attitude estimate that minimizes the error associated with the attitude transformation matrix. By doing so, the attitude estimate satisfies the Wahba optimality criterion [2]. Whereas satellites often require continuous attitude determination for communications links, instrument protection and alignment, and power generation, the CST position determination algorithms may be interrupted without these risks. In order to resume position determination, the CST requires only power and algorithm initiation. Because the CST function need not be cycle time-critical, many different attitude estimation algorithms meet the CST's operational requirements.

B. Digital Star Imaging

The fundamental concept that underlies CST operation is that a user's local position can be determined by observing and analyzing the stars in the night sky. This idea is by no means new; sailors, explorers, and navigators alike have used the stars to traverse the Earth for thousands of years. Therefore, it is natural that the first step in the local position determination process is to photograph the night sky, in this case using a digital imaging sensor. The two most commonly used digital imaging sensor classes are the charged couple device (CCD) and the complimentary metal oxide semiconductor (CMOS). Although both CCD and CMOS sensors are pixelated metal oxide semiconductors, the two sensors differ in readout technique [3]. When a CCD exposure is complete, the charge accumulated in the pixel array due to photon exposure is transferred to an output structure, which converts the charge to a voltage before it is sent to the camera's microprocessor. In the case of CMOS sensors, the charge to voltage conversion takes place at the pixel-level. This difference in readout technique results in significant performance disparities between the two sensor types. Although care should be exercised when selecting the most appropriate sensor type for a flight instrument, both CCD and CMOS sensors were considered allowable for research purposes.

C. Star Identification

One of the primary requirements of the CST position determination algorithm is the knowledge of two corresponding sets of star vectors as described in the attitude determination introduction. These vectors are generated in two steps by the star identification process. In the first step, the digital star image is analyzed using a process called centroiding. As with any digital photograph, the digital imaging sensor

is a matrix composed of thousands of individual light receptors, known as pixels. The number of pixels that register light from a given star will vary according to the magnitude (brightness) of the star. The centroiding algorithm executes a center-of-light calculation for each star using the cluster of pixels surrounding each bright spot on the image. The center-of-light calculation is analogous to center-of-mass calculations with the only difference being that pixel intensities are substituted for mass values. The centroiding algorithm outputs image plane coordinates for each star. These results are combined with the optical characteristics of the camera system to generate a set of three-dimensional star vectors in the camera's reference frame.

The second step of the star identification process is the comparison of the centroiding output to a catalog of reference star vectors. Although there are many different techniques to compare the digitally imaged stars to the catalog stars, all of the techniques should output the desired result — a set of reference star vectors that correspond to the star vectors generated by the centroiding code. Once the star identification process is complete, the attitude of the camera may be estimated.

D. Terrestrial Orientation Parameters

One of the primary reference frames used in the local position determination algorithm is the Earth Centered Inertial (ECI) reference frame. In the ECI frame, the coordinate system's origin is located at the center of the Earth, the z-axis is aligned with the Earth's spin axis, the x-axis points directly at the intersection of the Equator and Prime Meridian in the direction of the vernal equinox, and the y-axis completes the right-handed orthogonal set. The ECI reference frame is important because reference star catalogs list stellar coordinates in terms of two angles, right ascension and declination. The right ascension and declination angles are measured with respect to

the ECI frame and a given date, or epoch.

Although the ECI frame will often be referred to as the inertial frame in this work, naturally occurring forces on Earth perturb the orientation of the ECI reference frame. Corrections for these perturbations are made possible by highly accurate observation-based orientation parameters and predictions for the ECI reference frame reported by several scientific institutions including the United States Naval Observatory (USNO) and the International Earth Rotation Service (IERS). These parameters are often referred to as the Earth Orientation Parameters (EOPs). When the EOPs are known, the orientation of the ECI frame is well-established, and correlation with the reference star catalog can be assured.

E. Thesis Objectives

As previously noted, the CST offers an attractive alternative to GPS-type systems for navigation on the Moon and Mars. In order to prove the efficacy of the instrument, the CST's local position determination methods must first be demonstrated on Earth. The following objectives represent the contributions of this CST research effort.

1. **Elimination of the Zenith-Orientation Constraint**. The zenith-orientation constraint is an artifact of the mathematical development in [1]. The addition of a sensor to the CST instrument that can provide information regarding the relative orientation of the optical axis with respect to the local zenith direction enables the implementation of an additional attitude transformation that corrects for the misalignment. This approach eliminates the zenith-orientation constraint, and thereby, greatly improves the functionality of the CST.

2. **Proof-of-Concept CST Instrument Design and Fabrication**. In order to fully test CST functionality, it was necessary to design and fabricate a proof-

of-concept instrument. The proof-of-concept design is capable of testing a wide array of cases in the design envelope (zenith-aligned as well as off-axis alignments). Although this design should not be considered representative of the overall appearance or accuracy of a CST flight model, the proof-of-concept design provides the experimental setup required to demonstrate CST functionality and reveals important design issues for future models.

3. **CST Functionality Experiments**. The fabrication of a proof-of-concept instrument makes real-world experiments possible. The CST test program includes experiments in multiple geographic locations, various orientations with respect to the local zenith direction, and multiple test dates. By varying each of these parameters (location, orientation, and time), enough data was generated to complete an analysis of CST functionality.

4. **CST Error Source Analysis**. A properly functioning CST instrument outputs its local position and bearing. The value of the CST therefore becomes a function of the accuracy of the position determination output. In order to fully understand the factors that contribute to CST accuracy, research was conducted to analyze error sources and their impact on CST functionality. Special attention was given to mechanical design factors, optical axis alignment, and time dependence.

F. Thesis Organization

The thesis begins with the development of the basic mathematics that are fundamental to the CST algorithms (Chapter II). Although this development will be similar to the mathematics in [1], there are several important corrections to that work, without which the CST output would be erroneous. Following the basic theoretical develop-

ment, a thorough treatment of the elimination of the zenith-orientation constraint will be presented. This treatment will provide solutions for single-axis offsets and dual-axis offsets as well as a method to correct for the atmospheric aberration effect. Chapter III will detail the proof-of-concept instrument design and fabrication phases. A complete analysis of the CST error sources follows in Chapter IV. Chapter V will focus on the experiments that were conducted to validate the functionality of the CST proof-of-concept instrument. The final chapter of this thesis will summarize the theoretical and experimental findings. Chapter VI will also briefly address future design concepts and improvements to the CST concept.

CHAPTER II

LOCAL POSITION DETERMINATION

This chapter will introduce the mathematical theory that enables local position determination. Much of the mathematics is drawn from [1], but important corrections to that work and the elimination of the zenith-orientation constraint make this development a more complete and accurate reference for the position determination mathematics. The chapter begins with a brief introduction into the star identification and centroiding processes before addressing the position determination mathematics.

A. Star Identification

One of the primary requirements of the CST position determination algorithm is the knowledge of two corresponding sets of star vectors. These vectors are generated in two steps by the star identification process, which begins with a digital star image. The star image is processed using a centroiding algorithm that determines the star coordinates on the imaging sensor. The centroiding results are combined with the optical characteristics of the camera system to generate a set of three-dimensional star vectors in the camera's reference frame.

The second step of the star identification process is the comparison of the centroiding output to a catalog of reference star vectors. Although there are many different techniques to compare the digitally imaged stars to the catalog stars, all of the techniques should output the desired result — a set of reference star vectors that correspond to the star vectors generated by the centroiding code. Once the star identification process is complete, the attitude of the camera may be estimated.

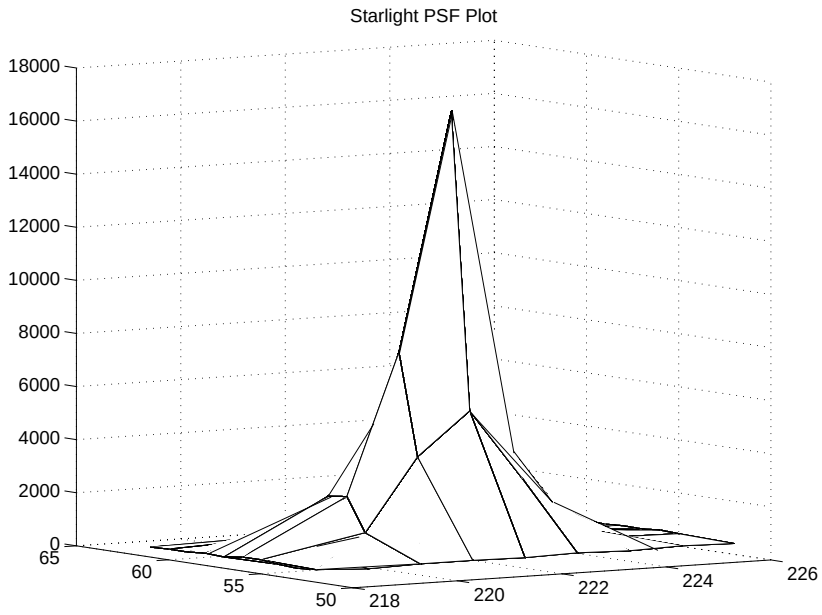

Fig. 1. Local starlight distribution on a CCD array

1. The Centroiding Algorithm

The primary responsibility of the centroiding algorithm is to calculate the photocenter for each potential star in the image array. Figure 1 shows a typical plot of a star's light distribution on a section of the imaging array. Although the majority of bright spots in star field images are in fact stars, the possibility of imaging planets and satellites or of having faulty bright pixels ("hot" pixels) in the array exists. For these reasons, the bright spots are not deemed stars until they have been identified as such. The general procedure of the centroiding algorithm, as adapted from [4], is given as follows.

1. Locate the brightest pixel in the image array: (x_m, y_m).

2. Using a topological search, identify all pixels surrounding (x_m, y_m) with intensity values greater than the gray-level threshold.

3. Determine the centroid location $(\hat{x}_m, \hat{y}_m)$ using Eq. 2.1.

4. Reset the intensity value for each pixel used in the $(\hat{x}_m, \hat{y}_m)$ centroid calculation to 0. NOTE: This step ensures that the m^{th} star will not affect other centroid calculations.

5. Repeat steps 1 - 4.

$$\hat{x} = x_m + \frac{\sum_{i=1}^{n}\sum_{j=1}^{n} x_{ij} I_{ij}}{\sum_{i=1}^{n}\sum_{j=1}^{n} I_{ij}} \qquad \hat{y} = y_m + \frac{\sum_{i=1}^{n}\sum_{j=1}^{n} y_{ij} I_{ij}}{\sum_{i=1}^{n}\sum_{j=1}^{n} I_{ij}} \tag{2.1}$$

Here, n is the number of pixels that surround the (x_m, y_m) pixel that have an intensity greater than the gray-level threshold, $(\hat{x}, \hat{y})$ is the star centroid location, I_{ij} is the pixel intensity value of the (i, j) pixel, and (x_{ij}, y_{ij}) are the x and y coordinates of the (i, j) pixel.

2. Star Identification Algorithms

The star identification algorithm represents one of the most vital components of the local position determination algorithm. Without star identification, the attitude of the camera body frame with respect to the inertial frame cannot be determined. Similarly, false star identifications will generate erroneous local position output. The two star identification algorithms discussed herein are examples of algorithms that the CST instrument could rely upon when fully automated. The first, Non-Dimensional Star ID, is advantageous because the star camera does not need to be properly calibrated in order for the algorithm to work [5]. This algorithm takes advantage of the fact that the first order geometry of star field triangles is unaffected by variations in the camera system's focal length and boresight offsets. Although this characteristic proves valuable for the initial star identification and subsequent optical calibration,

the Non-Dimensional Star ID algorithm's processing time requirements disadvantage its use as the primary star identification algorithm.

The second, and primary, star identification algorithm works by comparing the interstar angles for stars in a given star field image. The most advanced implementation of this type of star identification is the Pyramid algorithm [6]. The non-dimensional and interstar angle star identification algorithms would typically be employed in the following manner:

1. The initial star identification is accomplished using a non-dimensional star identification algorithm

2. The optical system parameters (focal length and boresight offsets) are calibrated using star field image vectors and their corresponding catalog vectors.

3. The optical parameters are passed to the primary star identification algorithm which then assumes responsibility for star identification tasks.

B. Attitude Transformations

1. Reference Frame Definitions

In order to develop the local position determination mathematics, one must begin by defining four reference frames: the body frame, the inertial frame, the Greenwich frame, and the local frame (See Figs. 2 and 3). The CST works by determining the attitude between these four distinct reference frames. It should be noted that *attitude* is defined as the relative orientation between two reference frames. A standard attitude notation convention allows the attitude of reference frame X with respect to reference frame Y to be written as $A^{X/Y}$. The following reference frame abbreviations will be used:

B - Body, or camera reference frame. **I** - Inertial (geocentric) reference frame.

G - Greenwich reference frame. **L** - Local reference frame.

Using these abbreviations and the aforementioned notation convention, the fundamental equation relating the four reference frames is

$$A^{B/I}A^{I/G} = A^{B/L}A^{L/G} \tag{2.2}$$

It is important to note the distinction between the local reference frame and the body reference frame. Whereas the local reference frame is located at the same latitude and longitude as the body reference frame, the body frame describes the local bearing and any misalignment that may occur between the camera and the local zenith direction.

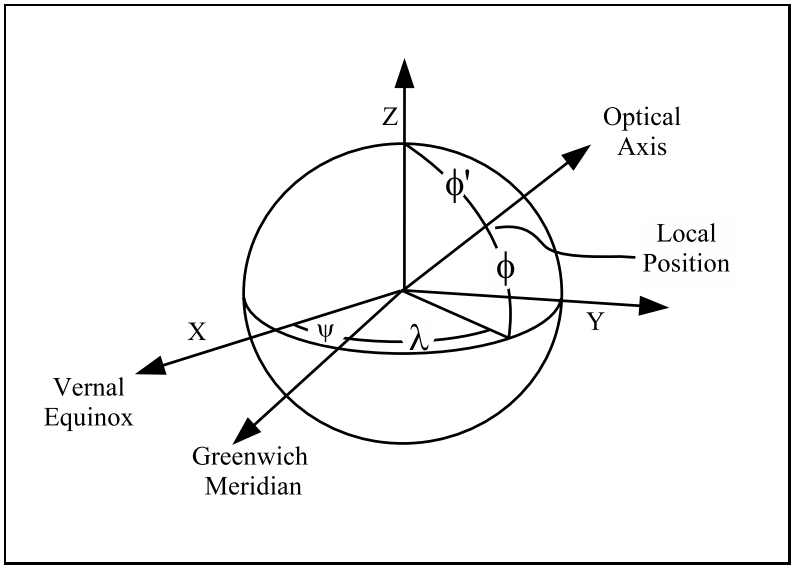

Fig. 2. The inertial reference frame for the CST

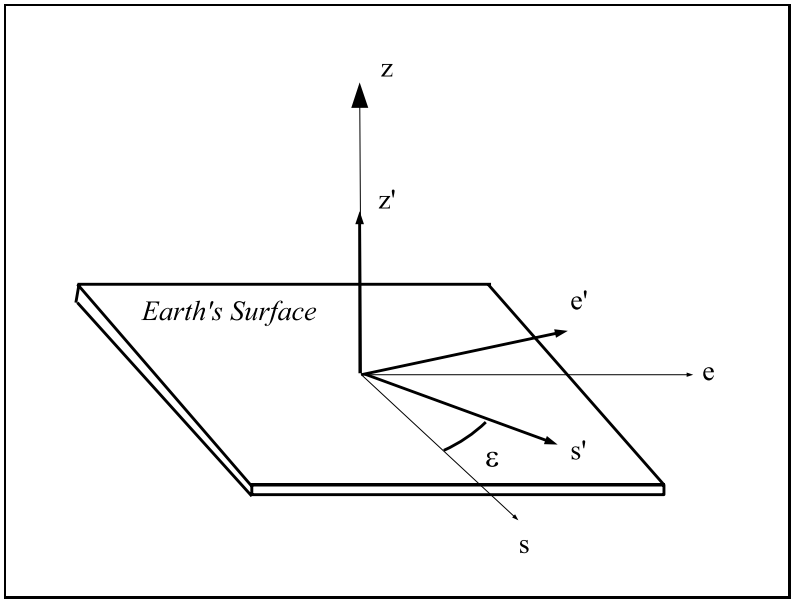

Fig. 3. The local reference frame for the CST

Figures 2 and 3 show some of the basic geometry associated with the four reference frames. The angles and directions shown in Figs. 2 and 3 are defined as follows.

- ψ is the angle between the vernal equinox (ascending node of the geocentric ecliptic) and the Greenwich Meridian. The angle, ψ, is known as a function of time.
- λ is the longitude.
- ϕ is the latitude.
- ϕ' is the complement of the latitude angle, ϕ .
- Optical Axis (**oa**) is the pointing direction of the camera. In Figure 3, **oa** is noted as $\mathbf{z}'$.
- ϵ is the angle between local South and the x-axis ($\mathbf{s}'$) of the camera body frame.

- $\{\mathbf{s},\mathbf{e},\mathbf{z}\}$ form an orthogonal coordinate system (the local reference frame) where $\mathbf{s}$ is local South, $\mathbf{e}$ is local East, and $\mathbf{z}$ is the zenith direction.

- $\{\mathbf{s}',\mathbf{e}',\mathbf{z}'\}$ form the camera body coordinate system where $\mathbf{s}'$ corresponds to the x-axis, $\mathbf{e}'$ is the y-axis, and $\mathbf{z}'$ is the z-axis.

One of the assumptions used in the CST mathematical development is that the optical axis of the camera (**oa**) is aligned with the zenith direction. Under this assumption, $\mathbf{z} = \mathbf{z}' = \mathbf{oa}$ in Fig. 3. The attitude of the camera body with respect to the local reference frame may then be written as

$$A^{B/L} \equiv R_3(\varepsilon) = \begin{bmatrix} \cos\varepsilon & \sin\varepsilon & 0 \\ -\sin\varepsilon & \cos\varepsilon & 0 \\ 0 & 0 & 1 \end{bmatrix} \tag{2.3}$$

Note that the solution for angle ε provides the Compass part of the CST. While the CST is primarily intended as a local position determination sensor, the local orientation information is a beneficial byproduct of the attitude mathematics. User interfaces for the compass information, ε, will be discussed in Chapter III. The local reference frame and the Greenwich reference frame are related using Eq. 2.4b.

$$A^{L/G} \equiv \quad R_2(\phi')R_3(\lambda) \quad = \begin{bmatrix} \cos\phi' & 0 & -\sin\phi' \\ 0 & 1 & 0 \\ \sin\phi' & 0 & \cos\phi' \end{bmatrix} \begin{bmatrix} \cos\lambda & \sin\lambda & 0 \\ -\sin\lambda & \cos\lambda & 0 \\ 0 & 0 & 1 \end{bmatrix} \tag{2.4a}$$

$$A^{L/G} \quad = \begin{bmatrix} \cos\phi'\cos\lambda & \cos\phi'\sin\lambda & -\sin\phi' \\ -\sin\lambda & \cos\lambda & 0 \\ \sin\phi'\cos\lambda & \sin\phi'\sin\lambda & \cos\phi' \end{bmatrix} \tag{2.4b}$$

In order to establish the attitude of the Greenwich reference frame with respect

to the inertial reference frame, one must account for the nutation and precession of the Earth's spin axis as well as small corrections for the polar motion of the Earth. In this development, the rotation matrix, NP, accounts for the precession and nutation of the Earth, ψ is defined graphically in Fig. 2, and the polar motion is accounted for by the W matrix. The exact form of the NP and W matrices will be studied in Chapter II, Section B.2. The $A^{G/I}$ matrix is given as

$$A^{G/I} = NP \cdot R_3(-\psi) \cdot W \tag{2.5}$$

Although all four matrices in Eq. 2.5 are functions of time, the classic time dependency notation has been omitted for simplicity. The three unknown parameters of the position determination algorithms are ϕ, λ, and ε. These parameters can be solved using the following manipulation of Eq. 2.2.

$$A^{B/L}A^{L/G} = A^{B/I}A^{I/G} = A \tag{2.6}$$

It should be noted that the product of $A^{B/I}$ and $A^{I/G}$ is known; $A^{B/I}$ is determined from the star identification and attitude determination algorithms, and $A^{I/G}$ is the transpose of the $A^{G/I}$ matrix which is computed using Eq. 2.5 and the instrument clock. Therefore, all unknown parameters are contained in the left-hand side (LHS) of Eq. 2.6. The LHS of Eq. 2.6 may be written in terms of the unknown parameters by using Eqs. 2.3 and 2.4b as follows:

$$A^{B/L}A^{L/G} = \begin{bmatrix} C_\varepsilon & S_\varepsilon & 0 \\ -S_\varepsilon & C_\varepsilon & 0 \\ 0 & 0 & 1 \end{bmatrix} \begin{bmatrix} C_{\phi'}C_\lambda & C_{\phi'}S_\lambda & -S_{\phi'} \\ -S_\lambda & C_\lambda & 0 \\ S_{\phi'}C_\lambda & S_{\phi'}S_\lambda & C_{\phi'} \end{bmatrix} \tag{2.7a}$$

$$A^{B/L}A^{L/G} = \begin{bmatrix} C_\varepsilon C_{\phi'}C_\lambda - S_\varepsilon S_\lambda & C_\varepsilon C_{\phi'}S_\lambda + S_\varepsilon C_\lambda & -C_\varepsilon S_{\phi'} \\ -S_\varepsilon C_{\phi'}C_\lambda - C_\varepsilon S_\lambda & -S_\varepsilon C_{\phi'}S_\lambda + C_\varepsilon C_\lambda & S_\varepsilon S_{\phi'} \\ S_{\phi'}C_\lambda & S_{\phi'}S_\lambda & C_{\phi'} \end{bmatrix} \tag{2.7b}$$

where $C_x \equiv \cos x$ and $S_x \equiv \sin x$.

The compliment of the local latitude, ϕ', the longitude, λ, and the orientation, ε, can be computed directly from the attitude matrix, $A^{B/G}$. The longitude and local East direction are computed without quadrant ambiguity using the following equations and the fully defined matrix A, the RHS of Eq. 2.6.

$$\lambda = \arctan 2\left[A(3,2), A(3,1)\right] \tag{2.8}$$

$$\varepsilon = \arctan 2\left[A(2,3), -A(1,3)\right] \tag{2.9}$$

The compliment of the latitude is given by

$$\phi' = \arcsin\left[\frac{A(3,2)}{\sin\lambda}\right] \tag{2.10}$$

or alternatively,

$$\phi' = \arcsin\left[\frac{A(3,1)}{\cos\lambda}\right] \tag{2.11}$$

The latitude can be solved as

$$\phi = 90 - \phi' \tag{2.12}$$

The motivation to have two formulas for determining the latitude arises from

the discontinuities in the sine and cosine functions. The position determination algorithm should be designed to recognize the discontinuities and subsequently select the appropriate equation for the determination of ϕ'.

2. Earth Orientation Parameters

The $A^{G/I}$ attitude matrix is the most complex of the four attitude matrices in Eq. 2.2. The $A^{G/I}$ matrix is complex because it is influenced by a number of physical factors, some of which occur over long time spans and other factors that are neither completely understood nor predictable. This section begins with a brief description of precession and nutation, two effects that are relatively well understood. The next topic addressed is the determination of the Greenwich angle, ψ (See Fig. 2). Following the description of the Greenwich angle, a standard method for dealing with deviations from the predicted motion of Earth using the Earth Orientation Parameters (EOPs) is described. These deviations are referred to as the polar motion.

Two separate $A^{G/I}$ prediction models will be presented in this section. The first model is drawn from [7] and will be referred to as the Vallado model. Although named the Vallado model in this text for simplicity, the Vallado equations are reproductions of the well-established IAU 1976 Precession and 1980 Nutation conventions. The second model is drawn from [8] and will be referred to as the IERS 2000 model. In essence, both models predict the $A^{G/I}$ attitude matrix using the results of observation data curve-fitting. Very little difference exists between the mathematical form of each model, but some difference can be seen in the two treatments of the nutation-precession matrix. The slight numerical differences in the Greenwich angle calculation and the polar motion correction will not be examined. All of the material presented in this section is explained in detail in [7] and [8].

One well-established principal of celestial mechanics is that the attitude of the Earth with respect to the ecliptic plane changes with time. One of the dominant motions affecting this change in attitude is the precession of the Earth's spin axis. This motion is caused by gravity torques produced by the Moon and Sun. Due to this precession, the Earth's spin axis sweeps out a 23.45° half-angle cone every 26000 years. In addition to the precession of the Earth's spin axis, the ecliptic poles move with respect to time although much more slowly than the spin axis precession. The combined effect of these two motions is called general precession.

The predictable short-term deviation of the Earth's spin axis from its long term precession is called nutation. The nutation transformation is required to account for the periodic effects the Moon and Sun have on the Earth. Nutational effects have a period of roughly 19 years and a maximum displacement angle of 0.005°.

The nutation and precession component of the Vallado model can be written as the product of four rotation matrices as follows.

$$NP = R_1(-\alpha)R_3(-\beta)R_1(\gamma)R_3(\delta) \tag{2.13}$$

where the angles γ and δ are the angles that specify the location of the ecliptic pole in the given inertial frame, β is the ecliptic angle of precession, and α is the obliquity of the ecliptic. All of these angles are functions of the current time and may be solved using the following set of equations.

$$\begin{aligned}
\alpha &= (84381.4428 - 46.8388t - 0.0002t^2 + 0.002t^3)/3600 \\
\beta &= (-0.0431 + 5038.4739t + 1.5584t^2 - 0.0002t^3)/3600 \\
\gamma &= (84381.4479 - 46.814t + .0511t^2 + .0005t^3)/3600 \\
\delta &= (10.5525t + 0.4932t^2 - 0.0003t^3)/3600
\end{aligned} \tag{2.14}$$

Here, the current time, t, is found using

$$t = (JD - T_0)/Tcentury \tag{2.15}$$

where JD is the Julian Date at the current time, T_0 is the Julian Date at J2000 ($T_0 = 2451545$), and $Tcentury$ is the number of days in one century ($Tcentury = 36525$). The IERS 2000 model calculates the nutation and precession matrix as

$$NP = R_3(-E)R_2(-d)R_3(E)R_3(s) \tag{2.16}$$

where E and d correspond to the location of the celestial intermediate pole in the celestial reference system using the following transformation.

$$X = \sin d \cos E, \quad Y = \sin d \sin E, \quad Z = \cos d \tag{2.17}$$

The term, s, can be expressed in terms of X and Y using the following equation.

$$s(t) = -\int_{t_0}^{t} \frac{X(t)\dot{Y}(t) - Y(t)\dot{X}(t)}{1 + Z(t)} dt - (\sigma_0 N_0 - \Sigma_0 N_0) \tag{2.18}$$

Here, σ_0, Σ_0, and N_0 are coordinates of the celestial ephemeris origin and the ascending node of the equator at J2000. Again, the reader should consult [8] for the full definition of the variables used in this development. For the purposes of this research, the nutation and precession matrix was calculated directly from the X and Y variables using the following equation

$$NP(t) = \begin{pmatrix} 1 - aX^2 & -aXY & X \\ -aXY & 1 - aY^2 & Y \\ -X & -Y & 1 - a(X^2 + Y^2) \end{pmatrix} \cdot R_3(s) \tag{2.19}$$

where if formally defined as $a = 1/(1 + \cos d)$. In order to simplify the calculation, a was approximated as $a = 1/2 + 1/8(X^2 + Y^2)$.

Another component of the $A^{G/I}$ calculation is the determination of the Greenwich meridian angle. This angle is also referred to as the Earth rotation angle. The angle, ψ, is found using

$$\psi(T_u) = 2\pi(0.779057273264 + 1.00273781191135448T_u). \tag{2.20}$$

where T_u is amount of Julian time since J2000 using the IERS UT1-UTC correction. The final component of the $A^{G/I}$ is the polar motion correction.

In order to generate the most accurate local position coordinates, several factors must be considered in addition to general precession and nutation to properly calculate the Earth's orientation. These additional factors are natural forces that have a weaker effect than precession and nutation and therefore are a means to fine tune the local position calculation. For example, the Chandler Wobble is an effect that is often attributed to the thermal currents in the Earth's oceans. Although hypotheses exist to describe the various natural forces that affect $A^{G/I}$, a long-term model capable of predicting the effects does not exist. Until such a predictive model exists, accounting for the natural forces' effects will require adjustments made possible by scientific observations. The observation data is publicly released by the USNO and the IERS. These institutions also publish short-term prediction bulletins. Therefore, realtime local position determination must rely on a direct link to the EOP reporting services or the USNO EOP predictions. The general equation used to account for polar motion is

$$W(t) = R_3(-s')R_2(x_p)R_1(y_p) \tag{2.21}$$

where x_p, y_p, and s' are the polar coordinates of the celestial intermediate pole in the terrestrial reference system and the position of the terrestrial ephemeris origin on the equator of the celestial intermediate pole, respectively. The x_p and y_p values are fully

defined by summing the IERS reported values and two additional terms that address effects with periods less than two days as follows.

$$(x_p, y_p) = (x, y)_{IERS} + (\Delta x, \Delta y)_{tidal} + (\Delta x, \Delta y)_{nutation} \tag{2.22}$$

For the purposes of this research, the (x_p, y_p) quantities were assumed to be equivalent to the IERS reported (x, y) values. The s' term was approximated using

$$s' = -47\,\mu\text{as}\; t \tag{2.23}$$

where t is found using Eq. 2.15 and μas is the unit, micro-arcseconds.

The nutation and precession, Earth rotation angle, and polar motion offset matrices are combined to generate the $A^{G/I}$ attitude matrix according to the following equation.

$$A^{G/I}(t) = NP(t)R_3(-\psi(T_u))W(t) \tag{2.24}$$

The Vallado and IERS 2000 models both make use of Eq. 2.24 with the primary difference in the resulting $A^{G/I}$ due to the alternative nutation-precession model. The difference in the accuracy of the two $A^{G/I}$ models will be shown in Chapter V, Section B. It should be noted that several approximations and assumptions were made in order to simplify the IERS 2000 $A^{G/I}$ calculations presented in this section. In order to further increase the accuracy of the $A^{G/I}$ matrix, and thereby the position determination results, the full series expansions and complete predictions of the IERS 2000 model should be applied.

3. Geodetic Latitude Transformation

Although many drawings and models depict the Earth as a sphere, these representations are simplifications that must be addressed for the purposes of this research. Two

additional Earth models are the ellipsoid and the geoid. The ellipsoid model is more realistic than the spherical model and accounts for the Earth's equatorial bulge. The geoid model is the most accurate model and was constructed based upon local gravity measurements and digital elevation data. Whereas the geoid representation is closest to the physical geometry of the Earth, the ellipsoid (specifically, the World Geodetic System 1984 (WGS84) ellipsoid) is appropriate for the CST algorithms. The WGS84 Ellipsoid is identified as being a geocentric equipotential ellipsoid of revolution. An equipotential ellipsoid is simply an ellipsoid defined to be an equipotential surface, i.e., a surface on which the value of the gravity potential is the same everywhere. The WGS84 ellipsoid was generated using a combination of measurements including satellite radar altimetry, Doppler, satellite laser ranging, VLBI measurements, et cetera. For a complete description of the WGS84 system, please reference [9].

The use of the ellipsoid model gives rise to two distinct latitude angles as shown in Fig. 4. The geocentric latitude is the angle between the equatorial plane and the line connecting the observer's position and the Earth's center. The geodetic latitude is the angle between the equatorial plane and the line perpendicular to the ellipsoid at the observer's position.

Upon first inspection, a theoretical disconnect seems to exist when the $A^{G/I}$ attitude transformation is closely examined. The trouble arises when one considers the consequences of the gravity gradient effect. Due to the gravity gradient, the local gravity direction is perpendicular to the Earth's equipotential surface. This means that plumb bobs and gravity gradient instruments will report the geodetic zenith as the local zenith direction. Although Fig. 4 exaggerates the Earth's equatorial bulge and the gravity gradient effect, it is clear that the geodetic zenith and the geocentric zenith directions are different. How then, can the local position be accurately determined if no knowledge of the geocentric zenith direction exists? The answer

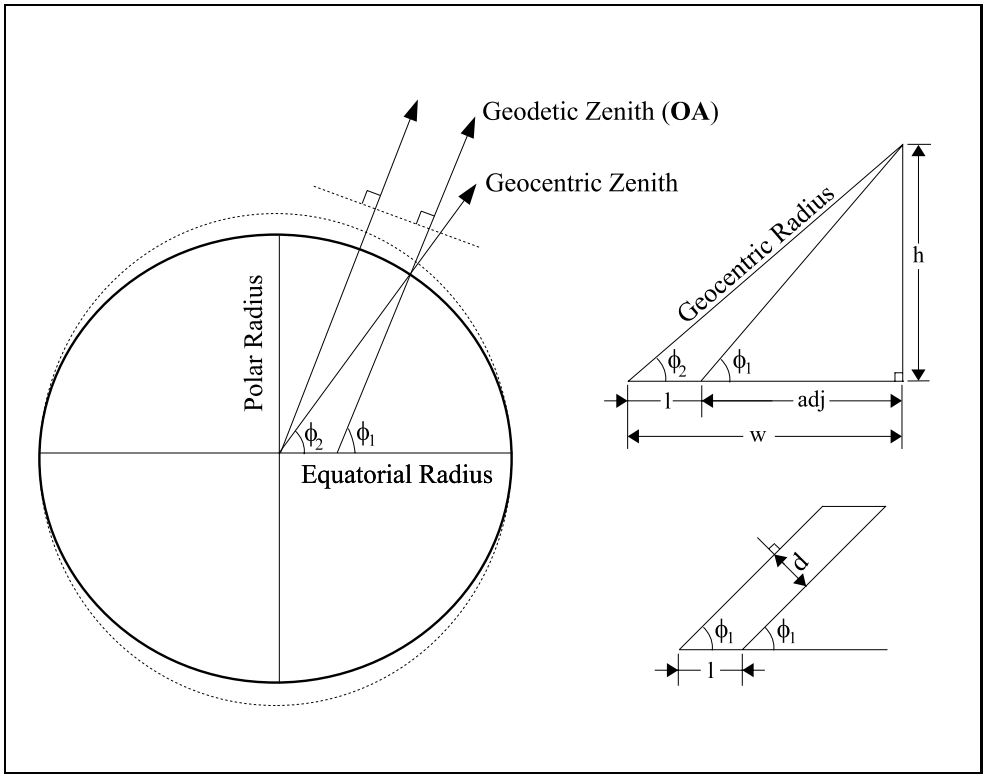

Fig. 4. Geodetic and geocentric latitude angles

to this question has two parts. First, the geodetic latitude must be converted to a corresponding geocentric latitude. Several convenient methods exist for performing the geodetic to geocentric conversion. One simple conversion formula, given in terms of the angles defined in Fig. 4, is

$$\tan \phi_2 = \frac{r_p^2}{r_e^2} \tan \phi_1 \tag{2.25}$$

where r_p is the polar radius, 6,356,755 meters, and r_e is the equatorial radius, 6,378,140 meters [1]. Secondly, the distance offset between the two observation vectors is inconsequential. This implies that two star images taken along parallel observation vectors but whose observation locations are separated by a given distance will show

the same star field if the position determination algorithms are to work. The following discussion validates this point.

In order to analyze the worst-case scenario, the geodetic latitude is chosen to correspond to the maximum orthogonal distance, d, between the observation vectors (See Fig. 4). When $\phi_1 = 45°$, $\phi_2 = 44.8076°$ (Eq. 2.25), the magnitude of the geocentric radius is 6.367×10^6 km and d is 21313 km. The orthogonal distance, d, may be analytically determined as follows.

$$h = (\sin\phi_2)\|\mathbf{r}_{geocentric}\| \tag{2.26a}$$

$$adj = \frac{h}{\tan\phi_1} \tag{2.26b}$$

$$w = (\cos\phi_2)\|\mathbf{r}_{geocentric}\| = l + adj \tag{2.26c}$$

$$l = (\cos\phi_2)\|\mathbf{r}_{geocentric}\| - \frac{(\sin\phi_2)\|\mathbf{r}_{geocentric}\|}{\tan\phi_1} \tag{2.26d}$$

$$d = l\ (\sin\phi_2) \tag{2.26e}$$

The relationship between the observation vector angles and the geocentric latitude is shown in Fig. 5. Using Eq. 2.26 and the distance to the nearest star outside our solar system (α-Centauri, 4 light years), the largest angular separation of the vector observations is approximately 10^{-4} arcseconds. Therefore, the error introduced by the geodetic latitude measurement is much smaller than the typical error magnitude of a star camera and can be considered negligible.

C. Off-Zenith Alignment

In the previous section, one of the primary assumptions is that the camera's optical axis is aligned with the local zenith direction. Although this assumption is perfectly valid and useful for the theoretical development of the attitude mathematics, the

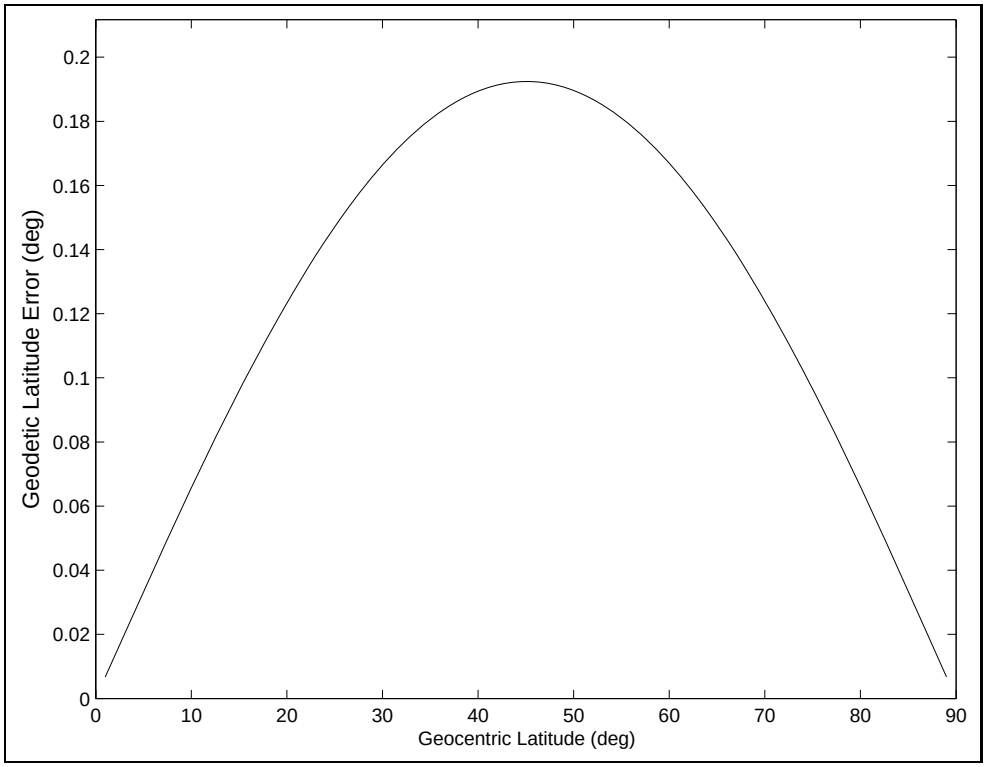

Fig. 5. Geodetic / geocentric latitude comparison

actual alignment or lack thereof in a real world environment requires attention. It is true that a rigorous design of the camera assembly may ensure zenith alignment, but a more reasonable approach would include sensors capable of measuring the optical axis, and therefore zenith offset angle, as part of the camera's operation. In this scenario, the offset angle could then be physically minimized thereby reducing the local position error.

One step beyond measurement of the optical axis or zenith offset angle is the incorporation of the angular offset measurement into the local position determination algorithm. In this section, the additional rotation matrix that is required will be introduced. Treatment will also be given to the effects of atmospheric abberation. In

order for this development to be valid, it is assumed that the optical axis or zenith offset angle is known (a sensor output) and that the rotation may be described by a traditional Euler rotation (the plane of rotation is perpendicular to one of the body axes).

1. Single Off-Axis Alignment

Let φ be the zenith offset angle of the optical axis. The camera body frame can then be related to the local reference frame by

$$A^{B/L} \equiv R_1(\varphi)R_3(\varepsilon) = \begin{bmatrix} 1 & 0 & 0 \\ 0 & \cos\varphi & \sin\varphi \\ 0 & -\sin\varphi & \cos\varphi \end{bmatrix} \begin{bmatrix} \cos\varepsilon & \sin\varepsilon & 0 \\ -\sin\varepsilon & \cos\varepsilon & 0 \\ 0 & 0 & 1 \end{bmatrix} \tag{2.27}$$

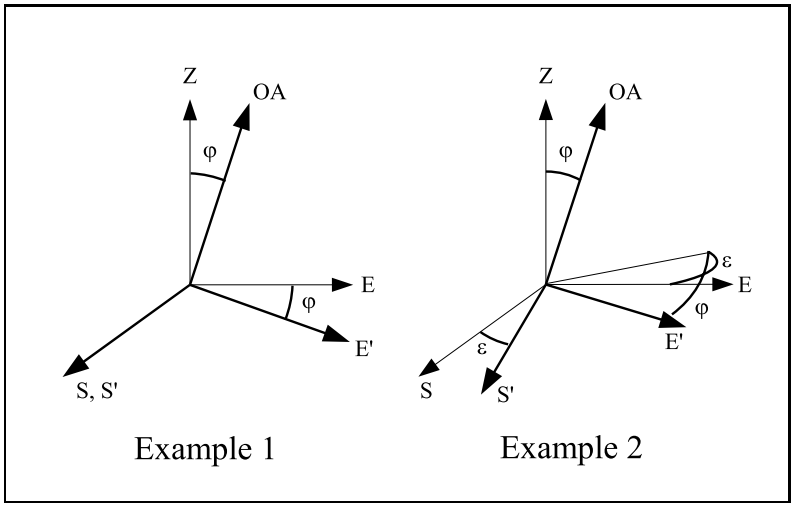

Fig. 6. The local reference frame with zenith angle offset

Figure 6 shows two examples of **oa** $\neq$ **z**. Example 1 depicts the special case where $\varepsilon = 0$, and Example 2 shows the general case where $\varepsilon \neq 0$.

2. Dual Off-Axis Alignment

While a single offset angle, φ, is sufficient to describe the difference between the optical axis and zenith, the fact that the rotation is quantified as $R_1(\varphi)$ constrains the camera body rotation to the 2-3 plane. This type of rotation can be guaranteed by a variety of mechanical designs, but such a constraint adds unwanted and unnecessary complexity to the final design.

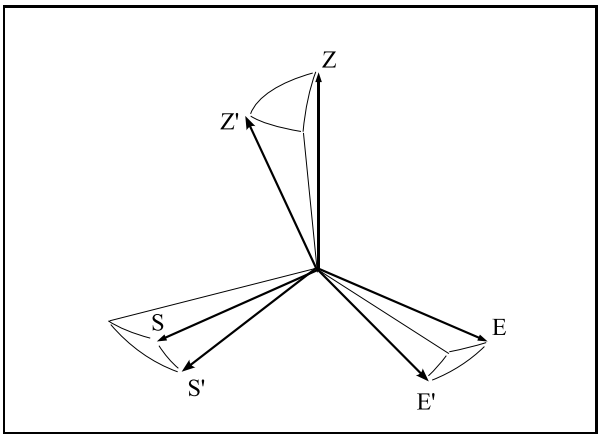

Fig. 7. Dual off-axis alignment

One solution that eliminates the rotation constraint is measurement of the angular offsets with respect to two axes of the camera body. Figure 7 illustrates the dual off-axis case. The two off-axis angular measurements, ξ and ψ, may be described using the familiar conventions of pitch and roll (See Fig. 8). If the two angles could be measured as sequential Euler angle rotations, the relationship between the camera body frame and the local reference frame would be the product of those rotation matrices. Complexities arise when the angles ξ and ψ are not related by successive Euler rotations but rather as independent angles measured with respect to the local reference frame. This situation is typical of a design that uses a dual-axis inclinometer.

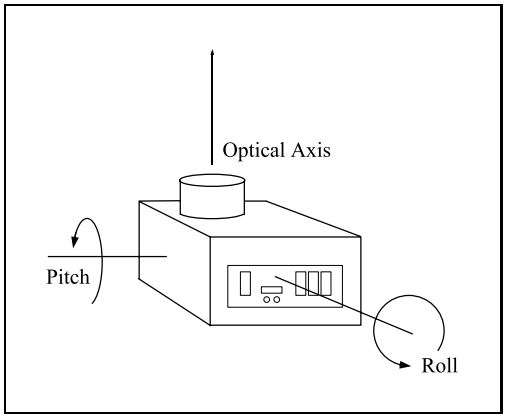

Fig. 8. CST pitch and roll angles

When ξ and ψ are measured independently with respect to the local reference frame, the attitude matrix, $A^{B/L*}$, must be determined where

$$A^{B/L} \equiv A^{B/L*} R_3(\varepsilon) = A^{B/L*} \begin{bmatrix} \cos\varepsilon & \sin\varepsilon & 0 \\ -\sin\varepsilon & \cos\varepsilon & 0 \\ 0 & 0 & 1 \end{bmatrix} \tag{2.28}$$

The geometric solution for the attitude matrix, $A^{B/L*}$, represents the intersection of two cones defined by the angular measurements ξ and ψ. The cones intersect at two points, one of which corresponds to the optical axis, **oa**. Figure 9 shows the two cones defined by ξ and ψ. *NOTE:* In the following development, the axes triad $\{\mathbf{s}, \mathbf{e}, \mathbf{z}\}$ will be noted as $\{\mathbf{x}, \mathbf{y}, \mathbf{z}\}$ and $x = \| \mathbf{x} \|$ $y = \| \mathbf{y} \|$ $z = \| \mathbf{z} \|$.

To begin, consider the equation of a circle in $\Re^3$.

$$x^2 + y^2 + z^2 = r^2 \tag{2.29}$$

Now, consider the case when the pitch angle is unknown. It is important to remember that the dual-axis inclinometer gives two independent angular measurements

as long as the inclinometer's measurement bounds are not exceeded. If the problem of cross-axis sensitivity is temporarily ignored, a given roll angle, ψ, can be paired with pitch angles, ξ, from $0 \rightarrow 2\pi$ radians to trace a circle with the optical axis, **oa**. Simple geometry yields the radius of the circle.

$$r = \cos\psi \tag{2.30}$$

Alternatively, it is known that the circle lies entirely on the plane where $x = \sin\psi$. This value can be substituted in Eq. 2.29 to give

$$y^2 + z^2 = r^2 = 1 - \sin^2\psi \tag{2.31}$$

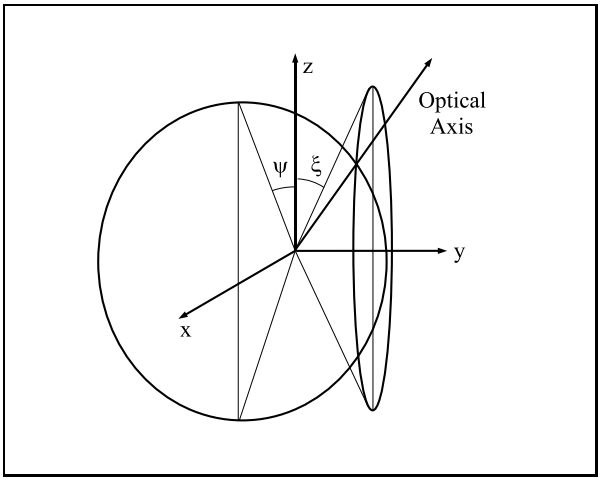

Fig. 9. The geometric solution for the dual off-axis alignment case

It should be clear that this development for a known roll angle could easily be translated to the case where the pitch is known and the roll is varied from $0 \rightarrow 2\pi$ radians. In this case, the circle lies on the plane where $y = \sin\xi$, and the resulting

equation for the circle traced by the optical axis is

$$x^2 + z^2 = r^2 = 1 - \sin^2 \xi \tag{2.32}$$

Naturally, both points of conic intersection will satisfy $x = \sin \psi$ and $y = \sin \xi$. All that remains is to solve for z. Substitution of the x and y constraints into Eq. 2.29 results in

$$z = \pm\sqrt{1 - \sin^2 \psi - \sin^2 \xi} \tag{2.33}$$

The combination of the constraints imposed by the inclinometer sensor and the physical practicalities of sky-viewing eliminate the possibility of a negative z solution. A negative z value would indicate an optical axis direction below the horizon. The optical axis vector is therefore

$$\mathbf{oa} = [\ \sin \psi \quad \sin \xi \quad \sqrt{1 - \sin^2 \psi - \sin^2 \xi}\ ] \tag{2.34}$$

Whereas the optical axis vector, **oa**, corresponds to $\mathbf{z}'$ (Fig. 9), $\mathbf{x}'$ and $\mathbf{y}'$ must be determined in order to solve for the attitude matrix, $A^{B/L*}$. Because $A^{B/L*}$ is orthonormal, the following equations must hold true

$$\begin{array}{lll} \mathbf{y}' \cdot \mathbf{z}' = 0 & \mathbf{x}' \cdot \mathbf{z}' = 0 & \mathbf{y}' \cdot \mathbf{x}' = 0 \\ \mathbf{y}' \times \mathbf{z}' = \mathbf{x}' & \mathbf{x}' \cdot \mathbf{x}' = 1 & \mathbf{y}' \cdot \mathbf{y}' = 1 \end{array} \tag{2.35}$$

One solution path begins by relating terms of the vector expression $\mathbf{y}' \times \mathbf{z}' = \mathbf{x}'$. The solutions for y_3' and y_1' are given by

$$y_3' = \frac{\cos \xi \sqrt{1 - \sin^2 \psi - \sin^2 \xi} - \cos \psi}{\sin \xi} \tag{2.36}$$

$$y_1' = -\frac{\cos \xi \sin \xi + y'(3)\sqrt{1 - \sin^2 \psi - \sin^2 \xi}}{\sin \psi} \tag{2.37}$$

Because $\mathbf{y}'$ should have unit length, the solution is

$$\mathbf{y}' = \frac{\mathbf{y}'}{\|y\|} \tag{2.38}$$

To complete the solution, $\mathbf{x}$ is known to be the cross-product of $\mathbf{y}$ and $\mathbf{z}$ both of which are now fully defined. The attitude of the camera body with respect to the local reference frame is

$$A^{B/L*} = \begin{bmatrix} \mathbf{x}' \\ \mathbf{y}' \\ \mathbf{z}' \end{bmatrix} = \begin{bmatrix} \mathbf{y}' \times \mathbf{z}' \\ \mathbf{y}' \\ \mathbf{z}' \end{bmatrix} \tag{2.39}$$

Due to the trigonometric terms in the solution path currently presented, singularities exist when either angle becomes 0° or 90°. The singularity that occurs when one angle becomes 0° is easily handled. In such a case, the single off-axis method is simply employed. Furthermore, the Compass Star Tracker is not intended for observations near the horizon which eliminates any concern for the difficulties near 90°.

The aberration of light must be considered for the dual off-axis case. In this situation, the angle between the optical axis and zenith must be determined. This angle corresponds to the Euler principal angle for the $A^{B/L*}$ attitude matrix. Using the Euler principal angle and principal axis parametrization of the attitude matrix, the angle is given by

$$\phi = \arccos \frac{\mathrm{tr}[A^{B/L*}] - 1}{2} \tag{2.40}$$

The principal angle, ϕ, found here is not to be confused with the local latitude. To complete the Euler principal rotation parametrization of $A^{B/L*}$, the principal axis, $\mathbf{e}$, must be determined. The components of the principal axis are

$$e_1 = \frac{A^{B/L*}_{23} - A^{B/L*}_{32}}{2\sin\phi} \quad e_2 = \frac{A^{B/L*}_{31} - A^{B/L*}_{13}}{2\sin\phi} \quad e_3 = \frac{A^{B/L*}_{12} - A^{B/L*}_{21}}{2\sin\phi} \tag{2.41}$$

The attitude matrix, $A^{B/L*}$, can then be expressed in terms of the principal axis and angle as

$$A^{B/L*} = I\cos\phi + (1-\cos\phi)\mathbf{e}\mathbf{e}^T - \tilde{\mathbf{e}}\sin\phi \tag{2.42}$$

where $\tilde{\mathbf{e}}$ represents the skew-symmetric matrix performing the vector cross-product.

$$\tilde{\mathbf{e}} \equiv \begin{bmatrix} 0 & -e_3 & e_2 \\ e_3 & 0 & -e_1 \\ -e_2 & e_1 & 0 \end{bmatrix} \tag{2.43}$$

3. Atmospheric Aberration

Snell's Law states that as light passes through two media of different density, light is refracted with respect to the boundary between the two media. One must consider Snell's Law (Eq. 2.44) when examining star field images taken from Earth's surface. The star light refraction due to the transition from the vacuum of space to the atmosphere of Earth is called *atmospheric aberration*.

$$n_1 \sin\theta_1 = n_2 \sin\theta_2 \tag{2.44}$$

The boundary between Earth's atmosphere and the vacuum of space cannot be described as a discontinuity, but it can be approximated as a series of parallel layers with density increasing toward the Earth. This effect, which causes stars to appear to have a greater local elevation, increases as the off-axis angle increases (See Fig. 10). For camera body alignments less than 45° from zenith, it is possible to calculate the angle of refraction, $\theta = \theta_1 - \theta_2$, according to the approximated equation

$$\theta = (n_2 - 1)\tan\theta_2 \tag{2.45}$$

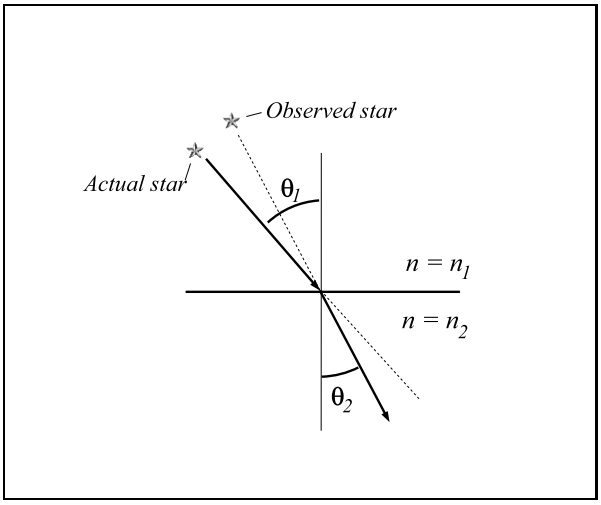

Fig. 10. The atmospheric aberration effect

where n_2 is the refraction index of air at sea level and θ_2 is the measured off-axis angle provided by the inclinometer. Figure 11 shows the amount of light refraction due to the Earth's atmosphere found using Eq. 2.45. The difference between the angular values shown in Fig. 11 and the exact solution of Snell's Law is approximately 10^{-6} degrees for $\theta = 0 \rightarrow 45^{\circ}$.

In order to incorporate the effect of atmospheric aberration into the local position determination algorithm, the aberration angle can be added to the off-axis rotation matrix as follows.

Single Off-Axis Alignment:

$$A^{B/L} \equiv R_1(\varphi)R_3(\varepsilon + \theta) \tag{2.46}$$

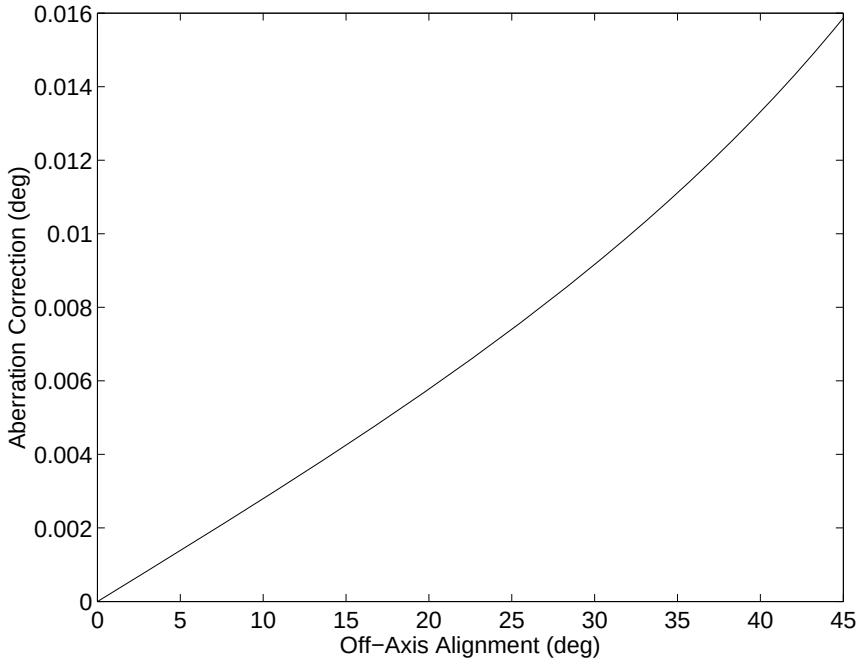

Fig. 11. Angular displacement due to atmospheric aberration

$$A^{B/L} \equiv \begin{bmatrix} 1 & 0 & 0 \\ 0 & \cos\varphi & \sin\varphi \\ 0 & -\sin\varphi & \cos\varphi \end{bmatrix} \begin{bmatrix} \cos(\varepsilon+\theta) & \sin(\varepsilon+\theta) & 0 \\ -\sin(\varepsilon+\theta) & \cos(\varepsilon+\theta) & 0 \\ 0 & 0 & 1 \end{bmatrix} \tag{2.47}$$

Dual Off-Axis Alignment:

$$A^{B/L*} = C(\mathbf{e}, \phi+\theta) \tag{2.48}$$

D. Summary of Position Determination Theory

This chapter was devoted to the various mathematical concepts associated with the local position determination problem. The fundamental mathematical development that spurred this research may be found in [1]. The research presented herein is im-

portant because it makes two significant contributions to the position determination problem: the elimination of the zenith-orientation constraint and the presentation of many theoretical corrections to the mathematics found in [1].

The zenith-orientation constraint was eliminated by incorporating a physical sensor in the camera design. The sensor is assumed to provide information regarding the attitude of the camera body with respect to the local frame. The off-zenith mathematics included single-angle and dual-angle cases. The effect of atmospheric abberation was also included in the off-zenith mathematics.

The theoretical corrections may seem inconsequential, but their effects are vital to accurate position determination results. The following list briefly illustrates the most important theoretical corrections.

- The latitude angle is now solved by determining the complement to the R_2 rotation angle in Eq. 2.4b.
- The local reference system is redefined as $\{\mathbf{s}, \mathbf{e}, \mathbf{z}\}$ in order to produce a right-handed coordinate set.
- The $A^{G/I}$ formulation is corrected by reordering the matrix multiplication and including the polar motion correction.
- The latitude angle solution is corrected to resolve sign ambiguities improperly addressed in [1].
- The values of the polar and equatorial radii are corrected.

Without these theoretical corrections, the position determination mathematics will not generate valid position coordinates.

CHAPTER III

PROOF-OF-CONCEPT COMPASS STAR TRACKER

The CST camera represents a proof-of-concept design intended to experimentally validate concepts introduced in [1] and the off-zenith alignment concepts introduced in Chapter II, Section C. Each section in this chapter describes a different instrument component, its requirements, and its integration into the system design. Following these descriptions, a detailed description of the CST design is provided.

A. Instrument Design

The proof-of-concept CST instrument was designed to be an inexpensive and easy to build platform capable of validating the theoretical position determination concepts. These design goals were justified in that this CST was solely intended as a proof-of-concept system. To this end, many commercial, off-the-shelf (COTS) parts were utilized in the camera construction. Whereas functionality of the completed system was always the primary consideration, the use of COTS parts greatly reduced design time and cost.

As testing of the proof-of-concept instrument progressed, strengths, weaknesses, and flaws of the original design became apparent. In fact, several of the original components were not incorporated in the NST data collection efforts because of component flaws, fabrication mistakes, or other unpredicted circumstances. This chapter will describe all facets of the original CST design and will also explain the modifications and additions where those departures from the original design occurred.

1. Imaging Sensor

In order for the CST to generate local latitude and longitude coordinates, a star field image is required. This image should have at least four centroidable stars that can be used in the attitude estimation algorithms. Although the stars in the night sky are relatively dim when compared to traditional photographic targets, many cameras exist that are sensitive enough to capture star field images. As with any camera, an exposure time must be selected that allows adequate light to reach the imaging medium. In digital photography, the exposure time is referred to as the integration time. If a camera is relatively insensitive to light, a longer integration time is required. If the integration time is too long, the sidereal rate of the Earth will cause the appearance of star streaks which are undesirable for the local position algorithms. Therefore, the primary imaging sensor design requirement is a digital sensor capable of producing star field images at an integration time short enough to prevent star streaks. The two imaging sensors included in the proof-of-concept design are the Philips ToUcam Pro and the SBIG ST-5C.

a. Philips ToUcam Pro

Astronomical CCD cameras commonly feature 12 to 16-bit resolution, but their cost and usability make them poor candidates for the CST design. Alternatively, standard web cameras (webcams) produce lower-grade, 8-bit images while offering a wide range of user features and low cost. Based on their usability and cost characteristics, webcams were judged to be the best option for the proof-of-concept design.

A Philips ToUcam Pro II web camera was selected for the CST design. The ToUcam features a Sony ICX098BQ Progressive Scan CCD Image Sensor (692(H) x 504(V) pixel array, 5.6 μm square pixels) controlled by a NEC μPD16510 vertical

driver. When paired with a 35mm focal length camera lens, the resulting FOV is 6.0°x 4.5°(see Eq. 3.1). Although the maximum integration time is factory preset at 1/25 second, the NEC vertical driver can be modified to allow integration times up to 3600 seconds [10]. The modification enables long exposures by selectively blocking the charge transfer pulses and stopping sub-pulses before they reach the driver.

In addition to the long exposure modification, the ToUcam imaging sensor and integrated circuit (IC) board were removed from the plastic camera housing. These components were reinstalled inside the CST camera body using fabricated parts, standoffs, and fasteners.

In its factory configuration, the ToUcam is controlled using a standard 5V universal serial bus (USB) connection. The CST design required additional inline D-Sub connectors along the length of the USB cable because of the light-tight location of the imaging sensor. Although additional electrical connections were required, the factory signal pin-out was maintained and the camera was directly controlled from the main computer.

b. SBIG ST-5C

Although a webcam CCD was always intended as the primary optical sensor for the reasons described above, an astronomical CCD camera was found available that could be piggy-backed on the CST camera body as a secondary image sensor. The astronomical CCD would be used as a redundant system helpful for doubling the system data output and assisting in the calibration of the primary webcam optics.

The astronomical camera that was found on-hand is a Santa Barbara Instruments Group Advanced ST-5C CCD Camera. The ST-5C is based on the Texas Instruments TC255 CCD (320(H) x 240(V) pixel array) and features an active cooling system. The ST-5C camera has 10 micron square pixels for overall dimensions

of 3.2mm x 2.4mm. This imaging sensor is relatively small and results in a small FOV (3.7°x 2.7°) when paired with the Nikon AI Series E lens (Eq. 3.1 and Table 1). Figure 12 is an example of a ST-5C image taken of Meissa and its neighboring stars. Meissa is one of the stars in Orion's belt. The image was produced using an integration time of 1.3 seconds. Although this integration time is rather long, the light sensitivity of the ST-5C camera is evident given the large number of stars captured in the image. Comparison of Fig. 12 to a reference star catalog confirms that Magnitude 9 stars are visible in the image. One should note that not all of the bright spots in Fig. 12 are stars. This image was taken as part of an experiment where dark frame subtraction was not used, and as a result, hot pixels populate the star field.

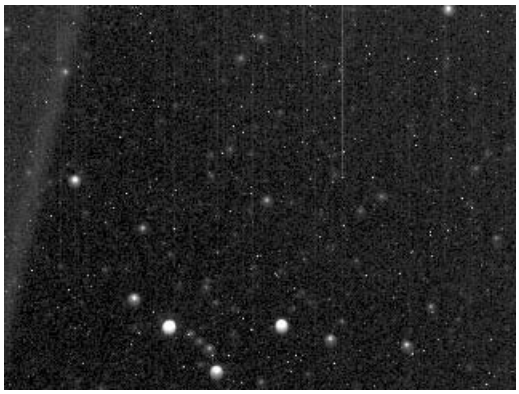

Fig. 12. An ST-5C image of Meissa

The ST-5C camera is relatively compact and fits atop the CST camera body quite easily, but it must be controlled via a camera processor module and an independent 110V AC power supply. The processor module connects to the main computer using a 25-pin parallel port cable. In the original proof-of-concept design, the ST-5C was intended to function as a backup to the ToUcam, but a electronics fabrication error

severely affected the ToUcam's performance. From that point forward, the ST-5C served as the only operational CST camera.

2. Optics

The choice of a camera lens for a star imaging instrument is dependent on the light sensitivity of the imaging sensor, the physical dimensions of the imaging sensor, and the desired integration time. The star identification code requires four centroided stars in order to eliminate the possibility of a false star identification. The imaging sensor must be paired with a camera lens that provides a wide FOV, which will guarantee the four star requirement. The FOV can be determined by

$$\theta = 2 * \arctan\left(\frac{d}{2f}\right) \tag{3.1}$$

where d is the chip size and f is the focal length of the lens. The lens should also have a wide aperture in order to allow the maximum amount of light to reach the imaging sensor. Care should also be taken to select a lens that is free of mechanical or optical defects that may result in image aberrations.

As mentioned in Section 1, there are two different cameras included in the proof-of-concept design. Accordingly, there are two different lenses used to produce star field images. The lenses chosen for the CST design were available on-hand and had desirable focal length and aperture parameters. The two CST lenses are shown in Table 1.

3. Inclinometer

The inclinometer is one of the most important CST components. When a zenith-aligned configuration is desired, the inclinometer allows the user to zero out the pitch and roll angles of the camera body, thus ensuring that the optical axis coincides with

Table 1. CST camera lenses

Lens Type	Focal Length (mm)	Aperture	Imaging Sensor
Nikon AF Nikkor	35-70	3.3	ToUcam Pro
Nikon AI Series E	50	1.8	SBIG ST-5C

the local zenith direction. In non-zenith configurations, the inclinometer measures the pitch and roll angles that are necessary inputs for the local position algorithms. The inclinometer provides knowledge of the camera body's orientation in the local frame, $A^{B/L}$, without which the CST cannot reliably function.

During the initial design phase, it was clear that the $A^{B/L}$ attitude matrix would have to be determined by an onboard sensor. What was not clear, however, was how accurate the onboard sensor would have to be in order to prove the theoretical concepts of the local position estimation algorithm. The theoretical error analysis (See Chapter IV) that would have shed light on this problem was conducted after the proof-of-concept instrument was built. Without specific design requirements, the search for an $A^{B/L}$ measurement device was arbitrarily limited to sensors that would be accurate below 0.1°, small in size, and inexpensive. Inclinometers are not the only instruments capable of measuring the camera body's pitch and roll angles. Inclinometers do, however, offer an attractive sensor option due to their accuracy and low cost.

The search resulted in the selection of a Spectron Instruments Spectrotilt™ SSY0091P dual-axis inclinometer. The SSY0091P sensor was small (2.5"×2"×1.5"), accurate (±0.06° accuracy, ±0.01° resolution), and inexpensive ($180). The plastic housing of the SSY0091P was mounted to the camera body using the two supplied

mounting holes, and its wiring harness was easily connected to the power supply and data acquisition board.

One of the primary constraints for any inclinometer is its measurement range. The SSY0091P is capable of measuring $\pm 20^{\circ}$ on each of its measurement axes. If either of these bounds are exceeded, the instrument begins to suffer from cross-axis sensitivity. Although the region of the sky near the zenith direction is best suited for position determination star images, there were several occasions when the cross-axis sensitivity constraints of the SSY0091P eliminated well populated star field targets.

The SSY0091P performance was regrettably poor. Although the inclinometer error analysis shows that the SSY0091P is not capable of determining location coordinates with sub-1 mile accuracy, the sensor was expected to report the pitch and roll angles reliably as long as the angles were within its measurement range. Thorough calibration testing of the inclinometer sensor revealed that not only were the dual-axis sensors not square to the sensor housing, they were not square to each other. Although the SSY0091P features null and scale adjustments for both axis sensors, the adjustment interface is inside the plastic housing. At this time, no attempt to disassemble and recalibrate the SSY0091P has been made. The non-orthogonal inclinometer sensors essentially eliminated the possibility of validating the off-zenith theory using only the CST instrument. The off-zenith theory could still be demonstrated and tested, but the analysis would require the use of additional tools (TheSky™ Astronomy Software).

4. Thermoelectric Cooling

As is common in most electronic applications, the digital star images are composed of signal (light from the stars) and noise (extra energy from non-star sources). One need only take a digital image with the lens cap in place to witness the pixel response

due to noise. Because many of the stars required for CST operation are rather dim, it is important to increase the signal-to-noise ratio (SNR) of the image so that the dim stars will be visible. The primary method of increasing star image SNR is to keep the imaging sensor as cold as its operating limits will allow. The ST-5C camera features a built-in active cooling system that can be activated and adjusted using the ST-5C software. The ToUcam Pro webcam lacks a cooling system, and therefore, a decision was made to cool the ToUcam as part of the CST design.

Among the webcam astronomy hobbyist community, imaging sensor cooling is predominately accomplished using Peltier cooling elements. These devices are named for the French scientist who is credited with discovering this cooling technique. Without going into detail, Peltier cooling occurs when an electrical current is applied to a semiconductor. The current passes between the n and p nodes of the semiconductor and results in a hot side and a cold side of the Peltier element (See Fig. 13). In a typical digital imaging setup, the imaging sensor is mated to the Peltier cold face using thermal grease. The thermoelectric cooling drains heat from the imaging sensor to the hot side of the Peltier element. The hot side must be connected to a heat sink and/or fan in order to dissipate the heat that accumulates.

Although a thorough thermal analysis would be most appropriate for sizing and selecting the cooling system components, the time constraints on the design process seemed reason enough to borrow from the webcam hobbyist community for their cooling system know-how. The result is a CCD cooling system comprised of a Marlow® DT12-6-01 Peltier element, thermally conductive, electrically insulating thermal grease, and a Thermaltake® Volcano Series A1889-01 heatsink / fan. The cooling system assembly is shown in Fig. 14.

The DT12-6-01 cooling element was tested by Spacecraft Technology Center (STC) lab technician Steven Summers using a range of input voltages. The test

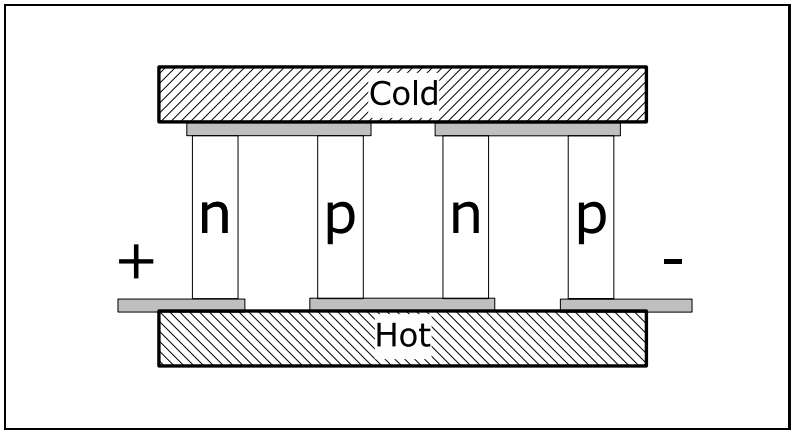

Fig. 13. The Peltier effect

was intended to determine the best operating values for the CST. The test results paralleled the DT12-6-01 data sheet performance curves and indicated that an input voltage of 7V would produce the most cooling allowable within the Sony ICX098BQ operating temperatures. In order to simplify the voltage regulation board, the 7V requirement was dropped in favor of an input voltage of 5V because that voltage would also be supplied to the inclinometer sensor.

5. Data Acquisition

The proof-of-concept CST instrument transmits its most important data, the digital star images, via the USB and parallel port cables associated with the two camera systems. The only sensor that does not directly transmit its measurements to the main computer is the inclinometer. The inclinometer sensor has no visible readout and, in any event, is located within the camera body. For these reasons, data acquisition becomes a design requirement for the proof-of-concept instrument. The primary constraints for this feature are compatibility with Labview™ software and a minimal amount of support hardware. The data acquisition system that was selected includes

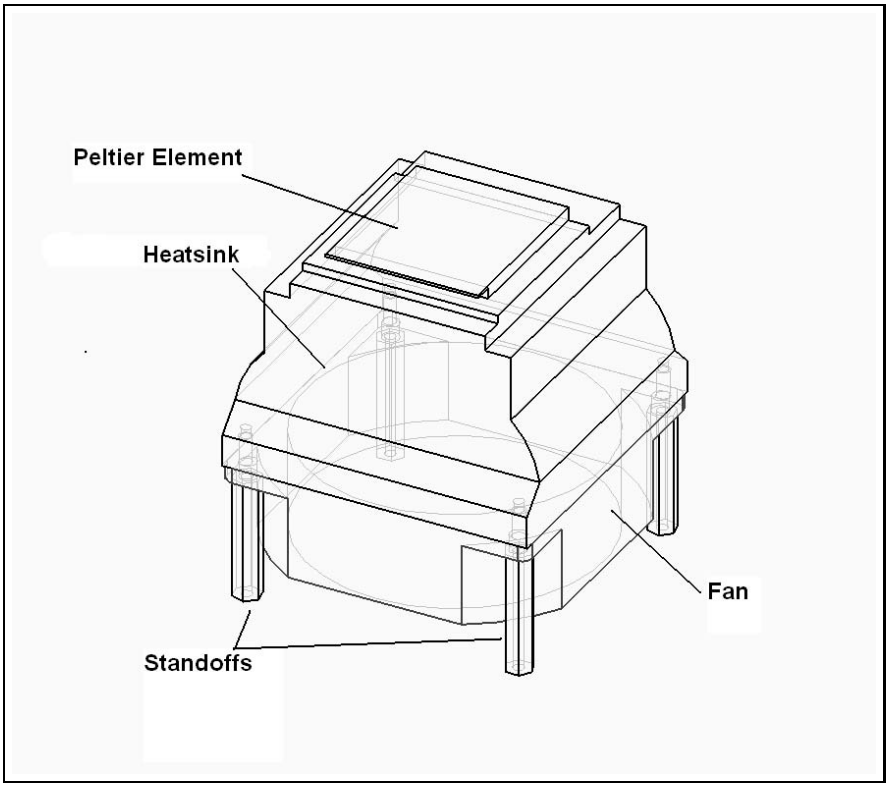

Fig. 14. Thermoelectric cooling assembly

the following National Instruments™ hardware (part numbers indicated in parentheses): a 68-channel connector block (77145-02), a 6' shielded ribbon cable (18638-01), and a PCMCIA card (778269-01).

The data acquisition system provides much more electronic signal monitoring and recording capacity than is required for the CST experiments. In fact, the majority of COTS data acquisition hardware is designed for a heavier work load. The inclinometer output requires only 2 of the 68 channels on the connector block, so one of the 66 spare channels was dedicated to a thermocouple that monitors the temperature of the imaging sensor via the Peltier element interface.

6. Voltage Regulator Board

The proof-of-concept CST has a limited amount of components that require power, but unfortunately the power needs of the heat sink, the cooling element, and the inclinometer are all different. Rather than supplying three different voltages to the instrument, it was decided that a voltage regulator board would be helpful in distributing the various voltages to the appropriate components. The highest power requirement for the CST instrument (12V DC) comes from the heat sink / fan assembly. Based on this requirement, 12V are input to the instrument via the banana jacks on the instrument panel. The power is routed to the voltage regulator board which then sends 12V to the heat sink and 5V to the cooling element and the inclinometer sensor. Although the desired input voltage for the cooling element was 7V, the lower voltage was chosen in order to simplify the regulator board and reduce its cost. The regulator board was designed by Steven Summers and manufactured by ExpressPCB™. A diagram of the voltage regulator board may be found in Appendix A.

7. Camera Body

The local position estimation capability of the proof-of-concept CST is made possible by the imaging and inclinometer sensors, the position determination algorithms, the data acquisition system, and the CPU. With this in mind, one might ignore the importance of the camera body which, upon first inspection, contributes little more than structure to the instrument design. Although the relative importance of the other instrument components may be greater, the camera body plays an important role by providing a structural framework that accommodates and allows certain aspects of the CST design to function. Without a camera body, the entire ToUcam

cooling system and optical assemblies could not work. Furthermore, the geometry of the camera body provides a convenient and well-known relationship between the instrument components. The most important of these are the relationships between the inclinometer sensor and the camera systems. Position determination in non-zenith alignments would be impossible if the relationships between the inclinometer and the camera systems were unknown.

The camera body, or housing, is constructed of seven aluminum plates. Six of the plates are exterior panels, and the seventh plate is an internal divider plate. Each plate was cut from 3/16" Aluminum 6061-T6 stock. The seven plates are fastened together by regularly spaced #2-56 screws.

The camera body is supported by four swivel levelling mounts. These mounts were originally selected because the swivelling feet can adjust to inclined and uneven surfaces on which the CST may be placed. During the course of the experimental testing, it became clear that the swivelling feet have too much mechanical "play" which makes small adjustments to the camera orientation difficult, if not impossible. On several testing occasions, the feet were removed in order to provide the CST a more stable base.

The overall dimensions of the camera body are roughly $8" \times 8" \times 4"$. The cost of materials for the camera body was approximately $80. All machining work was done at the STC by Patrick Marquardt. The following sections will address the design issues and requirements associated with the different camera body plates.

a. Instrument Panel

The instrument panel functions as a power supply and data transmission interface. Although the ST-5C camera functions are controlled separately, all of the original components of the CST instrument are represented on the instrument panel. The

instrument panel is shown in Fig. 15. The primary function of the instrument panel is to provide an interface for the power supplied to the CST instrument. From this panel, the user can activate the ToUcam cooling system, the ToUcam's long exposure mode, and the inclinometer power supply. All of the power supply switches are C&K® DF Series power rocker switches. This panel also provides space for the instrument's power supply input hardware, two Voltrex® solder-type banana jacks.

The two data transmission components on the instrument panel are the female USB and the 25-pin D-sub connector. Although the D-sub component is not connected to any signal lines at this time, it was incorporated into the design to allow easy expansion of the instrument functionality.

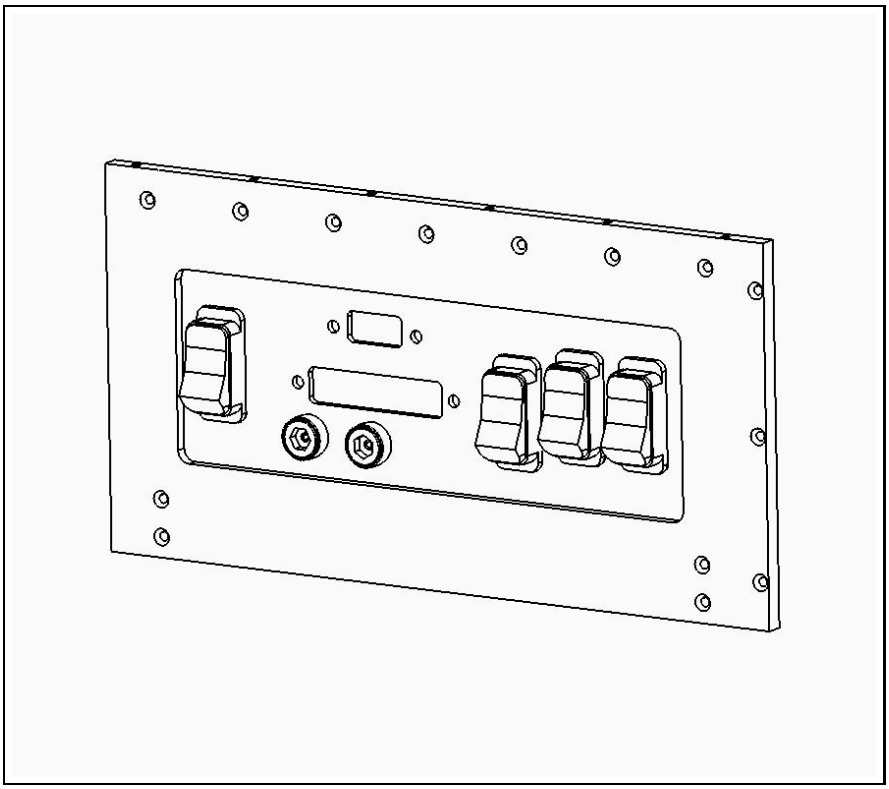

Fig. 15. CST instrument panel

b. Body Panel Features

The instrument panel joins three other side panels, a top panel, and a bottom panel to form the CST housing. As mentioned previously, each panel is cut from 3/16" aluminum stock and fastened to all adjoining panels using #2-56 screws. The hole patterns on the side panels were arranged in such a way that the computer controlled milling machine's cutting script could be repeated for each of the four parts.

The cooling system's air inlet and outlet ports are found on the right panel and the bottom panel, respectively. Each port is covered with an SPC Technology® aluminum fan filter screen. The access slot for the data acquisition connector block is also found on the right panel.

The primary features on the top panel are the cutouts required for mounting the ToUcam camera lens and adaptor. The ToUcam's factory lens was not appropriate for CST applications due to its limited FOV (See Section A2 of this chapter). In order to properly mate the Nikon lens to the imaging sensor, a lens adaptor was required. The lens adaptor serves to position the camera lens the proper distance from the imaging sensor and lock the lens in position. In the webcam astronomy hobbyists' community, one may easily find lens adaptors for the various webcam and camera lens combinations. A Mogg 840-Nikon lens adaptor was selected for the CST proof-of-concept instrument. These adaptors typically screw into the existing lens threads on the webcam body. Because the CST design discards the ToUcam's plastic housing, the Mogg lens adaptor was modified to connect directly to the CST top panel.

c. Divider Panel

The divider panel's main function is to create a light-tight compartment for the ToU-cam imaging sensor inside the CST housing. In this setup, the lower compartment is not light-tight. If the camera body enclosure was not divided in this way, a series of light baffles would be required at both cooling system ports. Because of the construction tolerances associated with the proof-of-concept instrument, the panel intersections that create the upper compartment may have gaps that would allow light in. These gaps may be filled with a permanent epoxy or a piece of electrical tape.

The divider panel also serves to constrain the location of the Peltier cooling element. As previously described, the cooling element is mated to the heat sink using thermal grease. Although this grease conducts heat efficiently, it does not glue the cooling element in place. Therefore, the divider panel was designed with a recess that would hold the cooling element in place.

8. Instrument Fabrication

The proof-of-concept instrument was fabricated by STC personnel Steven Summers and Patrick Marquardt. Steven Summers was chiefly responsible for the electronics modifications and installations whereas Patrick Marquardt completed the machining work. For a complete set of electrical and mechanical drawing sheets, refer to Appendix A.

B. Algorithm Architecture

This section outlines the various data and algorithms required for CST local position estimation. Many of the concepts required for the algorithms listed in this section

are given a more detailed treatment in other parts of this document. In such cases, the reader is encouraged to refer back to the appropriate section for a more thorough discussion of the theoretical concepts that constitute each algorithm. The architecture described herein should be considered appropriate for the proof-of-concept design. A description of the differences between the proof-of-concept algorithm architecture and flight model architecture will be presented in Section C of this chapter. A summary of the data inputs required for each algorithm is given in Table 2.

Table 2. Data inputs for the CST algorithms

Data	Dependent Algorithms
Digital Star Field Image	1, 2, 3, 4, 7
Reference Star Catalog	2, 3, 4, 7
Computer Timestamp	5, 7
Earth Orientation Parameters	5, 7
Inclinometer Output	6, 7

1. Centroiding Algorithm

The centroiding algorithm performs a center-of-light calculation for each star in the digital star image. This particular centroiding algorithm works recursively, i.e., it finds the brightest pixel associated with each star and then performs a topological search until it has registered all of the pixels above the grey-level threshold. The centroiding process is discussed at length in Chapter II, SectionA.

2. Batch Calibration Algorithm

The batch calibration algorithm uses least squares estimation to determine the focal length and boresight offsets of the camera system. The proof-of-concept implementation of this algorithm requires manual reference star input. If total automation of the CST instrument were required, this algorithm would rely on non-dimensional star identification to complete the optical parameter calibrations. A thorough discussion of the calibration process may be found in [11, 5].

3. Star Identification Algorithm

The proof-of-concept CST makes use of a rudimentary star identification algorithm based upon the interstar angles of the digital star image. This algorithm's construction was accomplished in a brute force manner, and the processing time suffers as a result. Whereas an automated CST would most definitely require reliable and robust star identification algorithms, the proof-of-concept instrument has been validated using manual star identification and the author's own star identification algorithm. A thorough treatment of interstar angle star identification is given in [6].

4. Attitude Estimation Algorithm

The attitude estimation algorithm specifically refers to the establishment of the relationship between the star vectors produced by the camera and the corresponding reference star vectors. The CST instrument utilizes the Second Estimator of the Optimal Quaternion (ESOQ-2) attitude estimation algorithm. The theoretical development of the ESOQ-2 algorithm is described in [12].

5. Earth Orientation Algorithm

The Earth orientation algorithm computes the attitude transformation for the Earth-Centered Inertial Reference System. This algorithm computes the angle, ψ, between the Greenwich Meridian and the Vernal Equinox direction. This algorithm also incorporates the effects of nutation, precession, and the observed Earth Orientation Parameters. The various concepts associated with these calculations may be found in Chapter II, Section B.

6. Local Orientation Algorithm

The local orientation algorithm is a short code that adjusts the $A^{B/L}$ attitude matrix based on the inclinometer output. In the event that the instrument is operated in a zenith-aligned configuration, this code is unnecessary for determining local position coordinates. The mathematics associated with this algorithm are discussed in Chapter II, Section C.

7. Local Position Estimation Algorithm

This algorithm combines the output from the aforementioned algorithms in order to determine the local latitude, longitude, and orientation. In actuality, this algorithm is shorter and simpler than any of the other algorithms. Because all of the grunt work associated with the various attitude estimates are carried out in the other algorithms, this code is simply comprised of 3 inverse trigonometric calculations. The mathematical equations required for this algorithm may be found in Chapter II, Section B. The overall algorithm architecture is shown in Fig. 16.

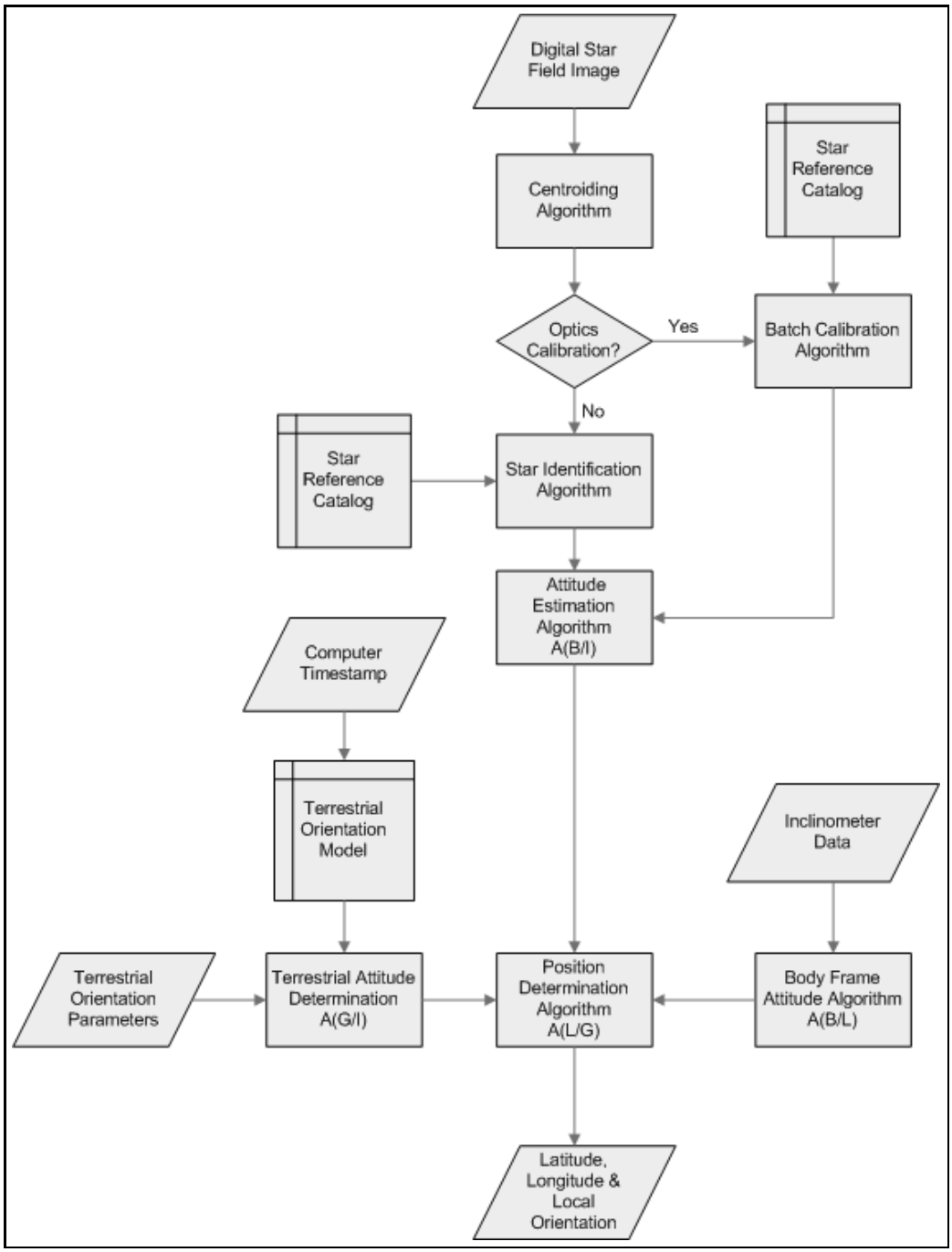

Fig. 16. CST algorithm architecture

C. Future Design Concepts

The proof-of-concept CST instrument was intended to validate the theoretical concepts associated with local position determination, and through experimental data, it has fulfilled that purpose. The proof-of-concept instrument has also been helpful in highlighting those critical design requirements that significantly affect the accuracy and precision of the output local position coordinates. With these lessons in mind, the three main areas of improvement for the next CST embodiment should be increased resolution and accuracy of the inclinometer sensor, reduced size of the instrument, and complete automation of the local position determination process. Improvements in each of these areas should be readily achievable; the technology required for hardware and software improvement already exists in academic papers and commercial products. These improvements should also be complemented by a camera body mounted graphical user interface that displays the local and orientation information. Although the form and substance of the next CST design will not be noted here, preliminary research indicates that position accuracy should improve by at least one order of magnitude.

CHAPTER IV

CST ERROR SOURCES

There are several error sources that affect the accuracy and precision of the CST's local position output. The CST error sources fall within two categories: electronic error and mechanical design error. This chapter will present the results of analyses and numerical simulations of the major CST error sources.

A. Electronic Error

The proof-of-concept CST is a relatively simple instrument that includes several pieces of electronic equipment. The primary electronic components are the camera system, the inclinometer sensor, the data acquisition board, and the computer's central processing unit (CPU). Due to factors such as signal noise and sensor accuracy thresholds, each of the electronic components contributes to the overall error of the CST. In order to quantify the electronic errors of the CST, an electronic error analysis is required. An electronic error analysis accomplishes two goals: the relative magnitude of each error source is determined, and the functional dependencies of each error source are identified. Although a complete error analysis would investigate the signal processing and signal transmission characteristics of the data acquisition board and the CPU, those errors are assumed to be several orders of magnitude smaller than the sensor errors described in the following sections. Each section will focus on a different electronic error source.

1. CCD Error

The attitude of the camera body with respect to the inertial frame is based on two sets of corresponding vectors: star catalog reference vectors and instrument body

vectors. The first set of vectors, the star catalog reference vectors, have an extremely small amount of error. A variety of star catalogs may be found with a cursory search of the Internet. Many star identification applications, including this research, use the Tycho-2 reference catalog. The Tycho-2 catalog has a position accuracy of ± 0.6 mas (mas = micro arcseconds) at J2000 and a proper motion error of ± 0.25 mas/yr [13]. This small error is due to the fact that the catalog information is the product of a multitude of accurate sensor measurements taken from Earth-bound and orbiting observatories over a period of years. The star catalog error is much smaller than the error associated with the instrument body vectors, which are based on the image centroiding results and the optical parameter calibrations. The reference vector errors are assumed to be negligible for the purpose of this analysis.

The instrument body vector error is due to errors arising from the star centroiding algorithm. The instrument body vector error may also arise if the optical parameters have not been properly calibrated. A thorough treatment of the performance and errors associated with various centroiding algorithms is given in [4], and optical parameter calibrations are discussed in [11]. Although the recursive centroiding algorithm used on the CST is efficient and straightforward, the algorithm is unable to differentiate between dark current noise and star light beyond what is accomplished by the algorithm's gray-level threshold. If the gray-level threshold is not properly set or if dimmer stars are included in the set of identified stars, error is introduced into the centroiding results and subsequently the instrument body vectors. Even when the threshold is properly set and only bright stars are imaged, the random distribution of dark current noise in the star image will introduce error into the centroiding results.

The second source of CCD error, improper optical parameter calibrations, is avoidable and correctable. The optical parameter calibrations include estimation of the camera focal length, the boresight offsets, and the imaging plane distortions. The

focal length and boresight offset calculations are of primary concern when initiating the camera's operation. Without knowledge of the focal length and boresight offsets, the star identification process must rely on a slower, non-dimensional approach such as the one described in [5]. The imaging plane distortions are not required for CST operation, but knowledge of the imaging plane distortions will reduce CST error. In general, the imaging plane distortions are much smaller in scale and require many more star images for proper convergence. Due to the small number of CST test images, the CST's calibration algorithm was not written to include imaging plane distortion calculations. The lack of imaging plane calibration should be remembered during the experimental centroiding error discussion.

In order to determine the error associated with the instrument body vectors, a loss function is defined according to the Wahba optimality criterion as

$$L(C) \equiv \frac{1}{2}\sum_{k=1}^{n} a_k |b_k - Cr_k|^2 = \lambda_0 - tr[CB^T] \tag{4.1}$$

where a_k are weighting coefficients, $\lambda_0 = \sum_{k=1}^{n} a_k$, and $B = \sum_{k=1}^{n} a_k b_k r_k^T$ is the attitude profile matrix. It should be noted that Eq. 4.1 is purely a function of the error angles between each body vector, b_k, and the corresponding vector associated with the estimated attitude matrix, $b_k' = A^{B/I} r_k$. For a set of n star vectors, the maximum error angle is

$$\theta_{max} = max(\arccos(b_k^T \cdot b_k')) \tag{4.2}$$

The maximum error angle can be equated to the maximum centroiding error on the imaging plane. Typical star trackers have centroiding accuracies better than 1/10 arcseconds [14]. CST experimental data shows worst-case centroiding accuracies near 12 arcseconds (See Chapter V, Section B). This centroiding accuracy is equivalent to 0.3 ST-5C pixels. This result suggests that imaging plane calibration would sig-

nificantly improve the accuracy of the centroiding results. It should be noted that a larger experimental data set would have allowed for the calibration of the imaging plane distortions. A full treatment of the imaging plane calibration process is given in [5].

A numerical simulation of the relationship between centroiding accuracy and local position estimation error is shown in Fig. 17. The numerical simulation used a focal length of 50mm and computed the average error for centroiding errors ranging from 0.01 to 0.30 pixels and standard deviations equal to 10 percent of the centroiding error. The average error was computed 2000 times for each centroiding error. It is important to note that the local position calculation was based upon ESOQ-2 attitude estimation using 2 Newton-Raphson iterations. Table 3 details the average error and error standard deviation for different Newton-Raphson iteration choices. The table illustrates that the overall accuracy of the attitude estimate improves significantly with subsequent Newton-Raphson iterations.

Table 3. Newton-Raphson iteration effects on position error

N-R Iterations	Average Error (miles)	Standard Deviation (miles)
0	3.0458	249.11
1	0.4545	5.56
2	0.4068	3.00

A Monte Carlo numerical simulation was conducted to show the results of 10000 error calculations using a focal length of 50mm, 2 Newton-Raphson iterations, and the experimental CST error (μ=0.3 arcseconds, σ=0.01 arcseconds). The simulation results are shown in Fig. 18. The resulting average position error is 0.370 miles.

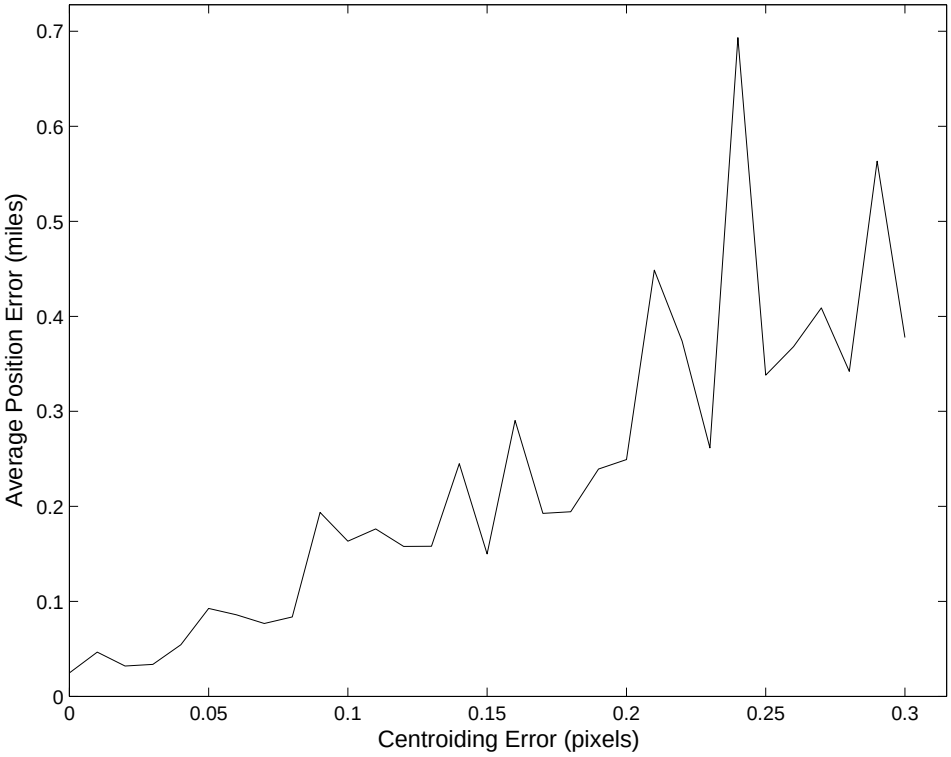

Fig. 17. Position estimate error due to centroiding error

2. Inclinometer Error

When the CST optical axis is not aligned with the local zenith direction, the inclinometer sensor measures the pitch and roll angles of the camera body in order to allow the CST to correct for the instrument orientation. Chapter II, Section C discusses the mathematics that is required when the camera's optical axis is not aligned with the local zenith direction. The theoretical development is theoretically valid, but it does not account for alignment error below the sensor measurement threshold, and misalignment of the optical axis vector is a highly sensitive source of CST error. The proof-of-concept CST design utilizes a Spectrotilt™ SSY0091P dual-axis inclinometer with $\pm 0.06^\circ$ accuracy and $\pm 0.01^\circ$ resolution. The 0.06° accuracy is reasonable for

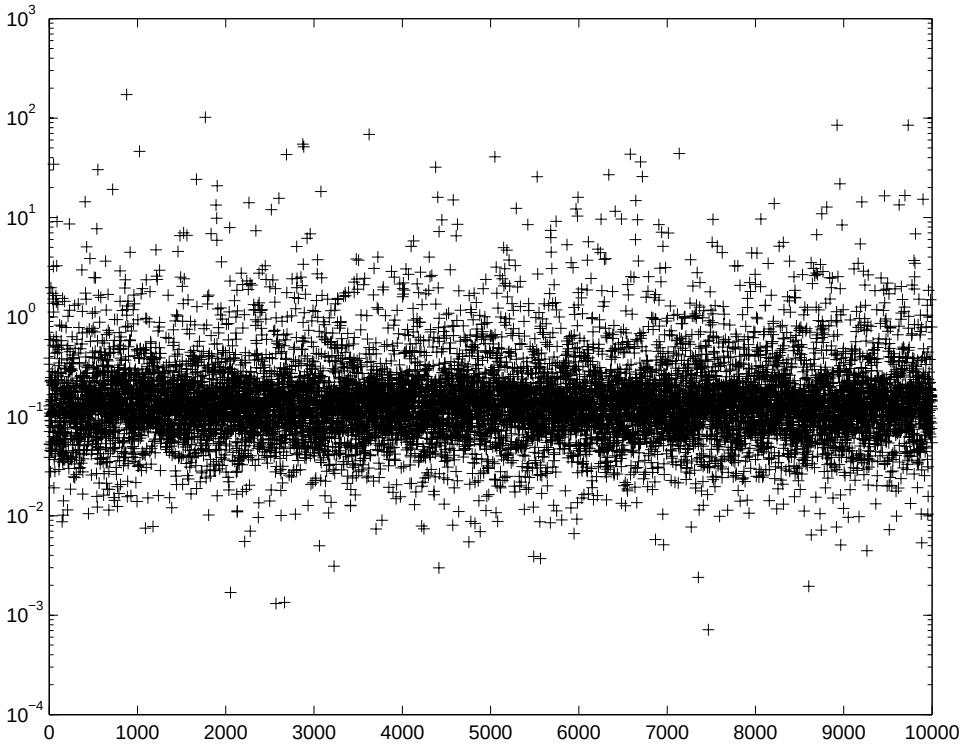

Fig. 18. Monte Carlo results for position error due to centroiding error

general alignment tasks but is unacceptable for precise local position determination requirements. The importance of measurements more accurate than the SSY0091P $\pm 0.06^\circ$ capability is shown in Figs. 19 and 20.

Figure 19 shows the effects that small deviations away from the local zenith direction have on the latitude and longitude estimates. In this figure, the attitude matrix for the local coordinates 30° North and 100° West is adjusted for pitch and roll rotations at angles below the accuracy threshold of the inclinometer sensor. In a practical experiment, these pitch and roll angles would be unknown because the inclinometer would output 0° for both measurement axes. When examining Fig. 19, please note that 30° geodetic latitude corresponds to a calculated angle, ϕ', of 59.833°.

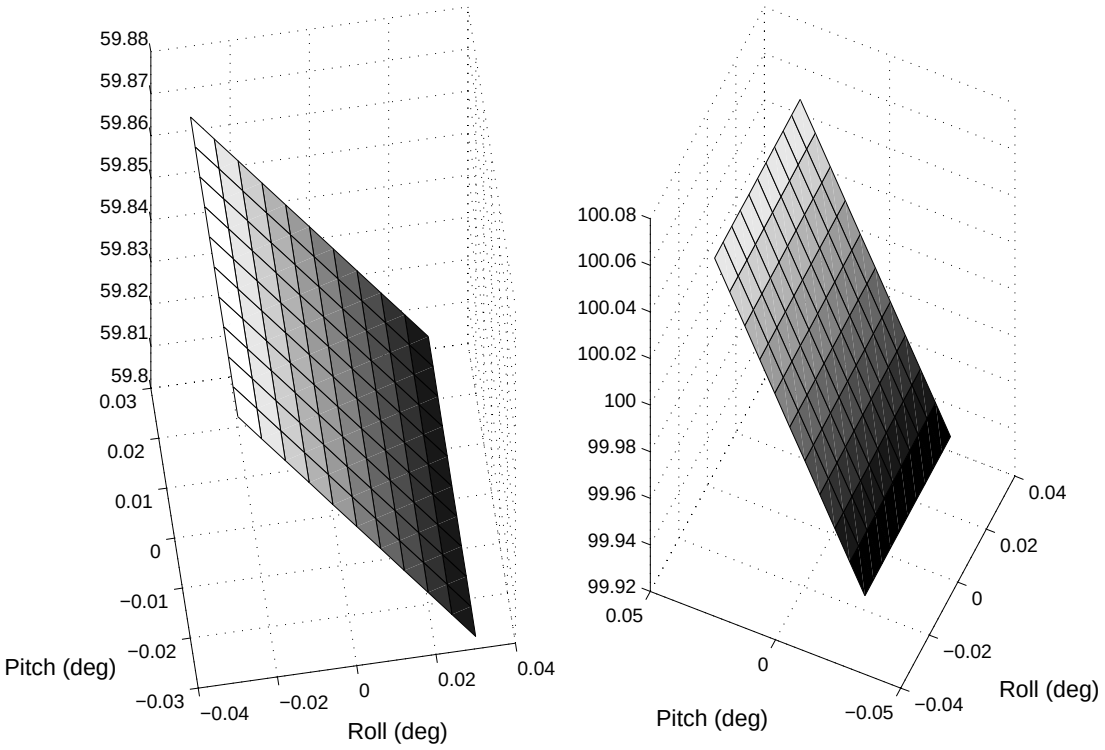

Fig. 19. Position estimate error due to inclinometer error

Although the rotation angles are smaller than 0.03°, the change in the estimated latitude and longitude position is significant. The latitude and longitude errors from Fig. 19 are combined to produce a contour plot of the total error associated with the inclinometer sensor threshold. Fig. 20 shows the combined error expressed as a distance given in statute miles.

The SSY0091P sensor will have true pitch and roll angles randomly distributed on the interval [-0.03°, +0.03°], where the interval is centered on the pitch and roll inclinometer output values. The 0.06° inclinometer measurement threshold produces an average error of 2.70 miles with a standard deviation of 0.16 miles. The maximum error on this interval is 4.65 miles.

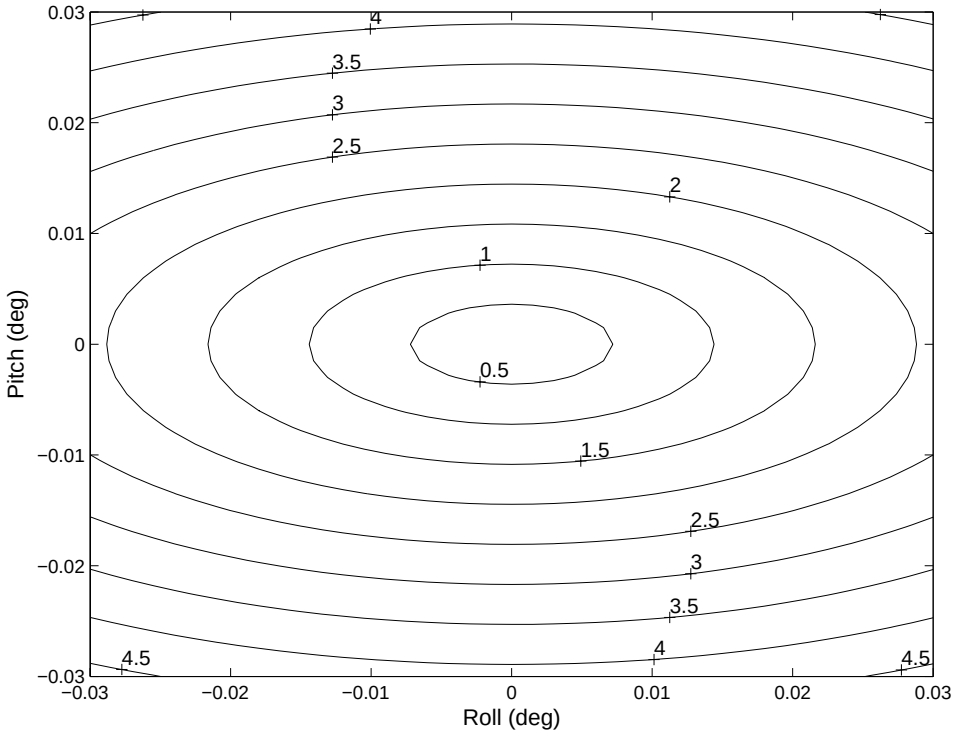

Fig. 20. Position error as a function of inclinometer misalignment

3. Image Capture Time Error

One of the position determination algorithm inputs is the image capture time. In the ideal case, the exact time of image capture would be known and no local position error would be generated. However, the proof-of-concept CST does not currently have a means to record the exact image capture time so consideration must be given to this error source. The most reliable and accurate means of dealing with the time dependence of the local position calculation would include synchronization of the computer clock with the U.S. Government Official Time and a fully automated machine-level transfer of the image capture time from the camera central processing unit to the algorithm processing unit. In the absence of these two requirements, effectively de-

termining the image capture time becomes somewhat arbitrary. Two options for determining the image capture time are given here. The first option is to save the image in the .FITS format and rely on the image timestamp recorded in the file heading. This timestamp is given in hr:min:sec format and is therefore only accurate to 1 second. The second option is to manually record the image capture time using a wristwatch. This method introduces human error and is unable to account for whatever time delay exists between initiation of the image capture command within the ST-5C GUI and the true image capture time.

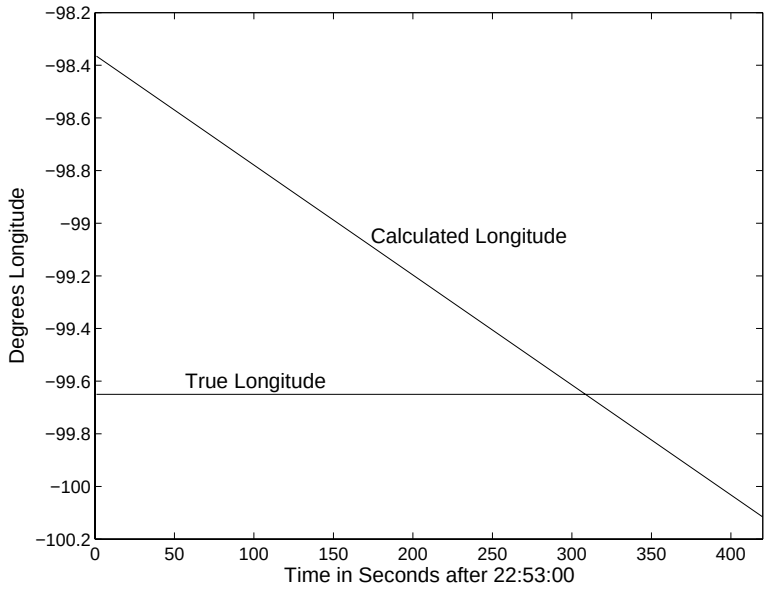

Fig. 21. Longitude calculation time dependence

Figures 21 and 22 illustrate the time dependence of the longitude and latitude position calculations, respectively. These figures were generated using actual test images taken at the Rojo Grande test site (See Chapter V). The reader should be aware that the inclinometer angles have not been incorporated in the local position estimation for these figures. Close attention to the scales of the y-axes of Figs. 21-22 reveals

that the longitude calculation is much more sensitive to time. The magnitude of the the calculated longitude time dependence in Fig. 21 is -4.17×10^{-3} deg/sec which is roughly equivalent to 1500 ft/sec. The magnitude of the latitude time dependence is 0.0089 ft/sec.

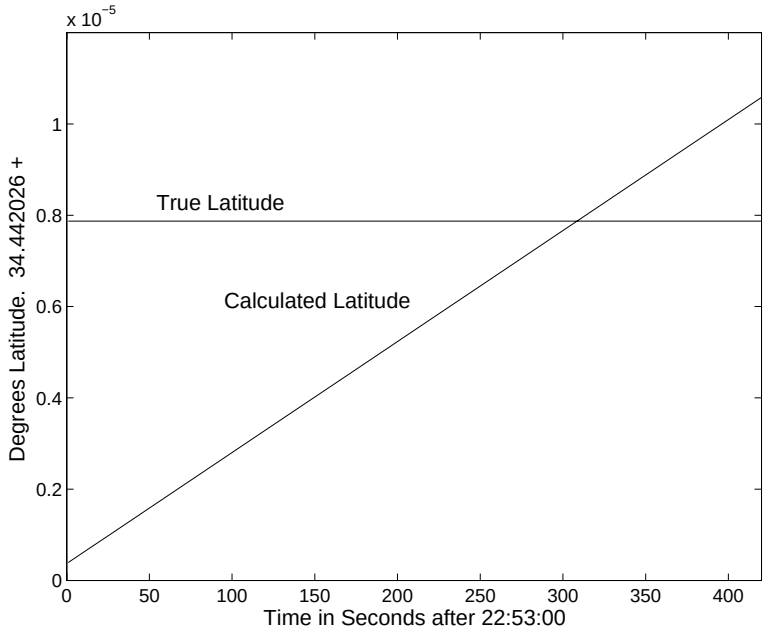

Fig. 22. Latitude calculation time dependence

It is important to remember the magnitude of the integration time used for the image capture when implementing the local position estimation algorithm. All of the experimental data used in this research was generated using a 1.3 second integration time. The image capture time algorithm input should correspond to the middle of the image exposure. Failure to account for half of the 1.3 second integration time will result in a position error of approximately 0.18 miles.

B. Mechanical Design Errors

The proof-of-concept CST was designed to be a simple and inexpensive instrument capable of proving the theoretical concepts outlined in Chapter II. One of the primary design requirements was to ensure proper alignment of the CCD imaging sensor, the camera optics, and the CST housing. If properly aligned, the imaging sensor would be parallel to the focal plane of the optics and square to the dual-axis inclinometer pitch and roll measurements. Due to construction tolerances associated with the CST fabrication, it is safe to assume some degree of optical axis misalignment. For a discussion of the errors that arise from optical axis misalignment, see Section A.

There are many different mechanical factors that can contribute to optical axis misalignment. Among these, the primary sources of mechanical misalignment are error tolerances in the CST housing construction, misalignments within the camera body, or a poor fit between the camera body and the camera lens. Secondary sources of misalignment include imaging sensor manufacturing errors or unequal cooling of the CCD.

Ideally any mechanical misalignment of the CST optical system could be determined experimentally and then corrected in the local position estimation algorithm. Unfortunately such a correction is limited by the inclinometer measurement threshold because the CST cannot distinguish between these two error sources. If the local position error is found to be outside the error cone associated with the inclinometer measurement threshold, the range of the possible mechanical misalignment angles can easily be calculated as $\theta = \epsilon \pm \alpha/2$ where ϵ is the optical axis error angle and α is the included angle of the inclinometer error cone. The position estimation algorithm should be written so that, in these cases, the minimum mechanical misalignment angle is corrected on subsequent iterations. Although this correction may not account for

the total mechanical misalignment, the misalignment angle will continue to decrease with each measurement iteration where $\epsilon - \alpha/2 > 0$.

The secondary error sources associated with the imaging plane of the CCD will be ignored for the purposes of this analysis. Any manufacturing defects or thermal effects on the imaging sensor would typically be compensated by the optical parameter calibrations as previously stated.

CHAPTER V

EXPERIMENTAL RESULTS AND ANALYSIS

The two main goals of the CST research effort were the thorough analysis of the local position determination problem and the successful demonstration of the CST proof-of-concept instrument and algorithms. This chapter is dedicated to the experimental data, results, and conclusions drawn from the CST tests. Not all of the CST experimental data is presented here. In fact, the early phases of the test program served more as learning experiences than data sources.

This chapter will begin with a description of the test locations, the general test procedure, and the lessons learned. The remainder of the chapter will focus on the data analysis and results.

A. CST Tests

1. Test Locations and Configurations

Once the CST proof-of-concept instrument was built, a test program was developed which would experimentally validate the theoretical concepts outlined in Chapter II. The test program was intended to exercise the three fundamental variables in the position determination problem: location, time, and camera orientation. If the camera could be successfully demonstrated in different geographic locations at different times using different camera orientations, the theoretical position determination concepts would be proven.

Ideally, the CST would have been tested at a wide range of latitude and longitude locations. Varying the latitude angle in the test program would have allowed for the analysis of the geocentric to geodetic angle conversion (See Chapter II, Section B).

Unfortunately, budget and time constraints precluded testing the instrument outside of Texas. Several other factors affected the choice of test location. These factors included weather, power availability, and property access. Three suitable test locations were chosen for the CST test program. The locations were the Rojo Grande Ranch in Mountain Home (1), a residential location in Fredericksburg (2), and a business location in College Station (3), Texas. The relative geographic locations of the three test sites are shown in Fig. 23.

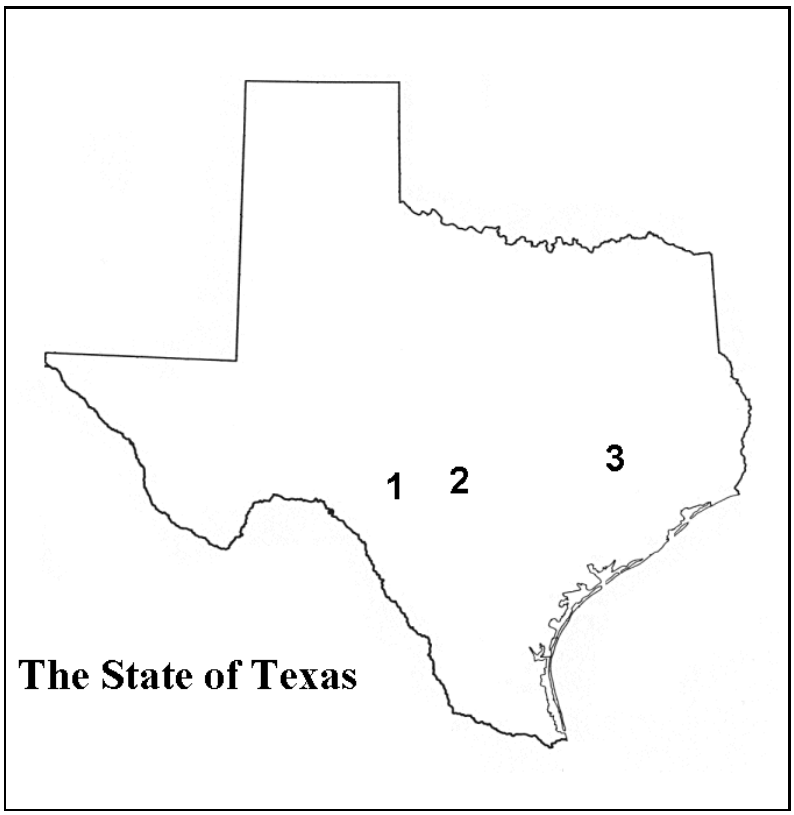

Fig. 23. Relative locations of the CST test sites

Because only one CST proof-of-concept instrument was built, varying the geographic location of the test sites meant that the time would vary as well. The tests

at the Rojo Grande test site and the Fredericksburg test site took place the nights of May 16 and 17, 2005, respectively. The College Station test occurred on the night of August 17, 2005.

The test plan dictated that the camera would be tested in zenith-aligned and off-zenith configurations at each test site. In general, the test procedure began with the setup of the CST camera, the power supplies, and the computer. Once all the equipment was connected and turned on, the inclinometer sensor was used to align the camera's optical axis with the local zenith direction and a series of images were captured. After the zenith-aligned images were taken, the camera was reoriented in various off-zenith configurations for the remainder of the testing. Unfortunately, the data acquisition card was not communicating properly with the Labview™ software during the College Station test and only off-zenith alignments were possible. The cause of this error, which has occurred on two other occasions, has not been determined. The number of images captured and the number of images with positive star identifications are summarized according to test location in Table 4. The lack of positive star identification for the Fredericksburg images is a result of camera alignment and inclinometer problems. These issues are discussed in the next section.

Table 4. CST test locations

Location	Zenith Orientation	Off-Zenith Orientation	Images Taken	Positive Star ID
1. Rojo Grande Ranch	✓	✓	20	14
2. Fredericksburg	✓	✓	15	0
3. College Station		✓	34	34

2. Lessons Learned

As with any developmental test program, the proof-of-concept CST night sky tests revealed several changes that should be incorporated in the next CST instrument design. These lessons learned deal with the optical axis alignment and the camera's user interface. By far, the most difficult aspect of the CST tests was alignment of the camera's optical axis. Optical axis alignment was a problem with zenith-aligned and off-zenith tests. This task proved difficult because of the camera's small FOV, the camera body design, and the inclinometer's manufacturing defects.

The primary challenge of obtaining zenith alignment was due to the inclinometer's manufacturing defects and the camera body design. Because the inclinometer's dual-axis sensors were not perpendicular to each other, it was nearly impossible to reach a zenith-aligned configuration using adjustments to the camera leg heights. Any change in the leg heights in the pitch direction would disturb the alignment of the camera roll angle and vice versa. Even if the inclinometer sensor had worked properly, alignment would have been difficult due to the four-leg design of the camera body. This problem could be solved by mounting the camera body on two hinged adjustment planes that directly correspond to the camera's pitch and roll directions. Many camera tripods feature exactly this type of mounting hardware. In the case of the CST mount, the hinged planes would require a means to make fine-tuning adjustments in order to increase the accuracy of the position determination output. The hinged planes design would be relatively simple and inexpensive. The time-savings accrued during testing would more than justify the work required to design and fabricate this type of mounting system.

The off-zenith alignment problems were caused by the camera's small FOV. The ST-5C camera's FOV is small, and most, if not all, of the stars in the captured

digital image are invisible to the unaided human eye. In essence, the test operator receives no alignment "feedback" from the captured star image. It is also virtually impossible to manually identify patterns of Magnitude 8 and 9 stars using astronomy software due to the large number of stars that exist in this magnitude range. These alignment issues are highlighted when the test operator wishes to image a specific star target. Not only will the test operator be challenged by the lack of image feedback, he will have no means of visually lining up the optical axis because of the camera body geometry. Put simply, the camera body lacks a peep-sight. The solution to this problem is to include a visual alignment tool on the next CST instrument design. Although a peep-sight would probably work, the simplest solution would be to attach a green laser pointer parallel to the optical axis on the camera body. Green lasers are commonly used by astronomy enthusiasts to point at stars in the night sky, and they are widely available on the commercial market ($80). A laser pointer would offer the test operator a quick and easy method to align the CST with any target in the night sky.

The second most important improvements to the instrument design would address the CST's data management and user interface. The proof-of-concept camera was not intended to be a stand-alone instrument, but data management and I/O interfaces would greatly improve the functionality of the CST. Ideally, the next CST design would incorporate the following data management and user interface features.

1. On-board computer for image processing and algorithm execution
2. Integrated data management system for inclinometer, camera, and clock output
3. Graphical user interface for local position and bearing output

If each of these design improvements were implemented, the CST could be reduced to a camera and a power supply instead of the four major hardware components

that are required for the proof-of-concept CST (power supply, CST, ST-5C controller, and laptop computer). Clearly, the optical axis alignment and user interface issues identified here could be addressed with straightforward improvements to the CST instrument design.

B. Analysis and Results

This section presents the results of the CST experimental data analyses. The centroiding accuracy analysis of the ST-5C star images is followed by analysis of the CST position determination accuracy.

1. Centroiding Accuracy

One of the factors that affects the position determination output is the accuracy of the centroiding algorithm. Poorly centroided stars will degrade the quality of the latitude and longitude calculations and may, in certain cases, prevent a positive star identification. This analysis is based on 8 of the 10 zenith-aligned images from the Rojo Grande NST. Two images were excluded from the analysis because they each had only two centroided and identified stars. Consider the following modified form of Eq. 4.2.

$$\theta_{avg} = \frac{\sum \arccos(A^{B/I} r_k \cdot b_k')}{k} \tag{5.1}$$

Equations 5.1 and 4.2 are used with the 8 Rojo Grande image data sets to construct Table 5. This centroiding accuracy analysis serves as the basis for the centroiding error analysis in Chapter IV, Section A.

Table 5. CST centroiding accuracy

	Average Error (arcsecs)	Standard Deviation (arcsecs)
θ_{avg}	6.93	1.85
θ_{max}	11.85	1.98

2. Position Determination Results

The primary aim of this research was to verify the local position determination concepts through experimentation, and for this reason, this section may be regarded as the crux of the research effort. This section will begin with a brief description of the experimental challenges faced in the CST test program and a few notes regarding the experimental data. The rest of the section will focus on the many ways that the experimental data was analyzed and how those results may be interpreted.

Experimental methodology dictates that a test environment isolate the test variable so that data variance or, for that matter, invariance may be directly attributed to the variable in question. In the case of the CST, this experimental requirement is more easily stated than accomplished. The latitude and longitude variables are dependent on the centroiding accuracy, the accuracy of the image capture timestamp, the knowledge of the Earth's orientation in space, and the accuracy of the instrument's inclinometer sensor. If conclusive test results are desired, each of these factors must be controlled to the fullest extent possible.

The most sensitive of the test variables is the instrument's inclinometer sensor output. The inclinometer output leads to the CST's orientation in the local reference frame, and it is therefore vitally important to the position estimation algorithms. In order to fully understand the complexities associated with this test variable, consider

an experiment where the instrument's orientation in the local frame is intended to be kept constant. In the outdoor environment where the CST operates, a multitude of natural factors (wind, temperature, non-rigid testing surface, etc.) virtually guarantee that the $A^{B/L}$ attitude matrix will vary with respect to time. The amount that the local orientation changes and whether those changes are measurable will significantly affect the results and the error of the local position estimation algorithms.

The position determination analysis is based on the star images captured at the Rojo Grande Ranch in Mountain Home and at the University Services Building in College Station. All of the images were captured using the ST-5C camera and were stored on the laptop computer's hard drive for subsequent processing.

The first data processing step was execution of the centroiding algorithm. After the centroiding algorithm had been run on each star image, the centroided stars were manually identified using TheSky™ astronomy software. The right ascension (RA) and declination (DEC) coordinates of each identified star were recorded in a database with the corresponding star centroid results. TheSky™ software allows the user to adjust the software's time and date settings thereby allowing the user to determine the stars' RA and DEC angles at the exact image capture time. The database of centroid results and (RA,DEC) coordinates was used to construct input data files for the main position determination algorithm sequence.

The position determination algorithm sequence requires four data inputs: the centroiding and star identification results, the image capture time, the Earth orientation parameters, and the inclinometer output. All of these data inputs were available to the position determination algorithm sequence except the inclinometer output (See Chapter III). Because the inclinometer data is invalid, the pointing direction of the camera had to be determined analytically. In this process, the testing location's latitude and longitude coordinates must be known. The pitch and roll angles of the

camera body can then be extracted from the attitude mathematics using the simple trigonometric constraints outlined in Chapter II, Section C. Once the pitch and roll angles have been determined, one can determine the Euler rotation angle and rotation axis according to the principal rotation theorem. Although this technique for determining the camera body's orientation works, it gives no allowance for the position error due to sources other than the inclinometer sensor. Therefore, timestamp errors, centroiding errors, and EOP errors are absorbed by the optical axis pointing direction calculation. Figures 24 and 25 show the principal angle solutions for the Rojo Grande and College Station images, respectively. The affect of the choice of $A^{G/I}$ model is shown in Fig. 25.

The first important observation that should be made concerning the principal angle solutions is the difference in the y-axis scales of Figs. 24 and 25. The standard deviation of the data in Fig. 24 is 0.002, and the standard deviation of the IERS 2000 solution data in Fig. 25 is 0.433. This obvious disparity is most likely due to the testing environments at the Rojo Grande Ranch and the College Station test site. At the Rojo Grande Ranch, the CST experimental setup included a very large, sturdy table on which the camera was placed. In College Station, the testing surface was a lightweight desk. The desk could easily have been bumped or disturbed by the test operator as he conducted the NST, and the data shows strong indication that the pointing direction of the camera was not kept constant in College Station. Although there is variance in the Rojo Grande principal angle solutions, the somewhat periodic trend of the data suggests that the time dependent $A^{G/I}$ matrix may be a factor.

In order to judge the accuracy of the principal angle solutions, TheSky™ astronomy software was once again employed. The software allows the user to identify the altitude (ALT) and azimuth (AZM) coordinates of a location on the celestial sphere in addition to providing RA and DEC coordinates. The appropriate altitude and

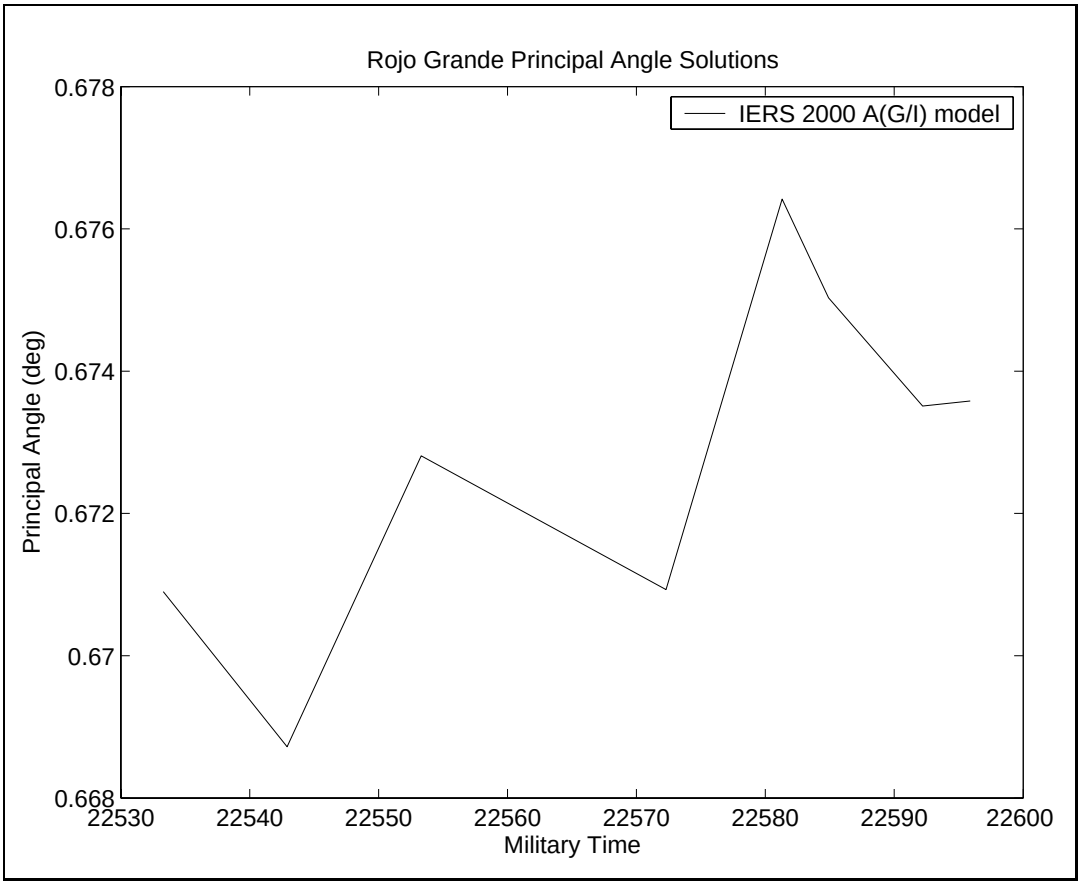

Fig. 24. Principal angle solutions for the Rojo Grande images

azimuth coordinates are found by matching the center of the test images with a location in software's sky model. If the principal angle solutions are correct, there should be close correlation between the principal angle and the altitude. Furthermore, the spikes that appear in Fig. 25 should correspond to changes in the pointing direction of the optical axis.

The optical axis pointing directions found using the astronomy software are very near the analytical principal angle solutions. The principal angle solution for the Rojo Grande image taken at 22:53:33 is 0.6709°. The altitude angle produced by the astronomy software and shown in Table 6 corresponds to a principal axis angle

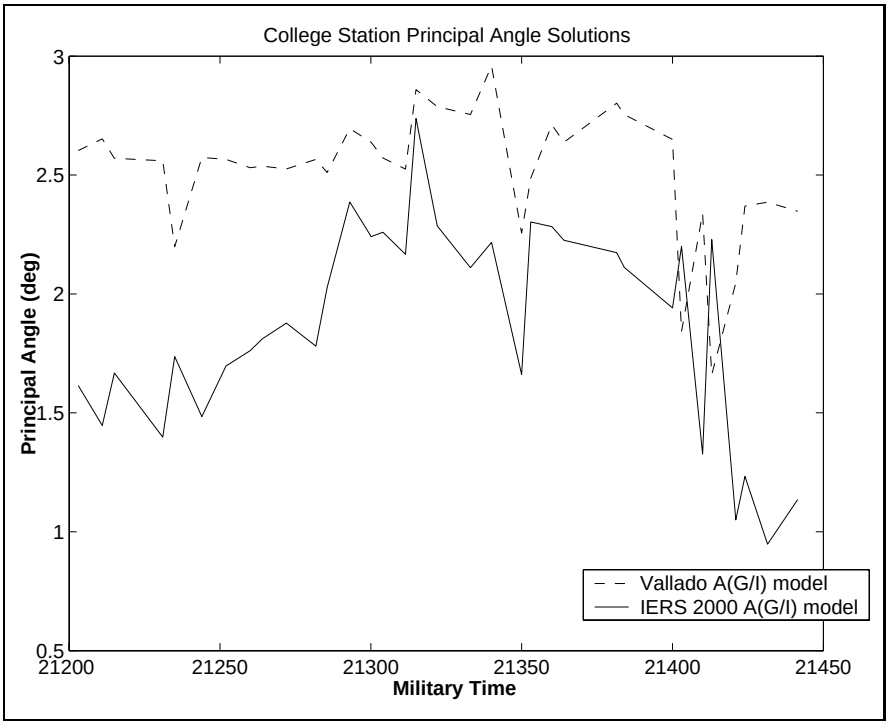

Fig. 25. Principal angle solutions for the College Station images

of 0.8308°, a difference of roughly 0.16°. The difference between the College Station angles is even smaller at 0.137°. The slight discrepancies between the principal angle solutions and the angles determined by the astronomy software are almost certainly a result of the error sources that the principal angle solution must neglect. These results strongly suggest that a functioning inclinometer would fully enable the position determination capability of the CST.

The software analysis also showed that the pointing direction of the camera changed during the course of the College Station testing, thereby explaining the spikes on Fig. 25. A sample of the results showing the change in the optical axis direction is given in Table 7.

To continue with the data analysis, TheSky™ software was used to determine

Table 6. CST optical axis pointing directions

Location	Time	ALT	AZM
Rojo Grande	22:53:33	88d 24m 43s	311d 00m 52s
College Station	21:20:30	88d 31m 20s	20d 00m 50s

Table 7. CST optical axis direction variation

Time	ALT	AZM
21:20:30	88d 26m 07s	27d 21m 22s
21:29:30	88d 22m 43s	26d 10m 39s
21:31:50	88d 23m 31s	28d 06m 07s
21:35:00	88d 23m 59s	27d 53m 57s
21:41:00	88d 25m 30s	27d 38m 36s

the optical axis pointing direction for the Rojo Grande test images. The optical axis direction was then used to construct the $A^{B/L}$ attitude matrix, thereby completing the position determination input requirements. The local position was calculated for the Rojo Grande test images using both $A^{G/I}$ models, and the results are shown in Fig. 26.

Two important conclusions can be drawn from Fig. 26. The first conclusion is that the position determination results are very precise which is a testament to the stability of the Rojo Grande test setup. The standard deviations of the two data sets are 0.3584 miles (IERS 2000 $A^{G/I}$ model) and 0.2976 miles (Vallado $A^{G/I}$ model). These results are encouraging considering that the instrument is a proof-of-concept

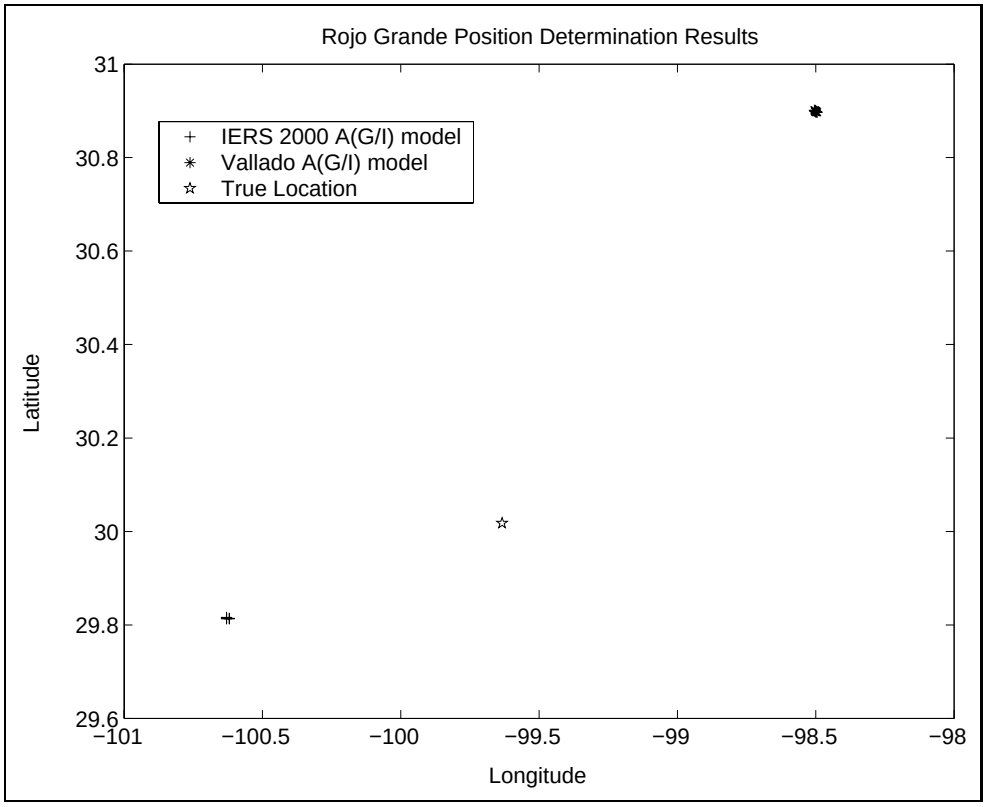

Fig. 26. Rojo Grande position determination results

model, the imaging sensor is not fully calibrated, the image capture time is only known to within one second, and the IERS 2000 $A^{G/I}$ approximation only includes the first five terms of the series expansion.

The second conclusion that can be drawn from Fig. 26 is that the $A^{G/I}$ matrix calculation is highly sensitive to its model fidelity. Although both $A^{G/I}$ prediction models are valid, the IERS 2000 model generates more accurate position coordinates even without its entire series expansion. Estimates of the position error were found using spherical geometry. The average error of the IERS 2000 position coordinates was 61.23 miles, and the average error of the Vallado $A^{G/I}$ model was 91.00 miles.

It is important to note that the Rojo Grande position determination analysis is

made possible by the stability of the test setup. The position determination algorithm sequence used the same $A^{B/I}$ matrix for each test image. This technique should not be employed for data sets where the optical axis pointing direction changed during the course of testing. This point is illustrated in Fig. 27.

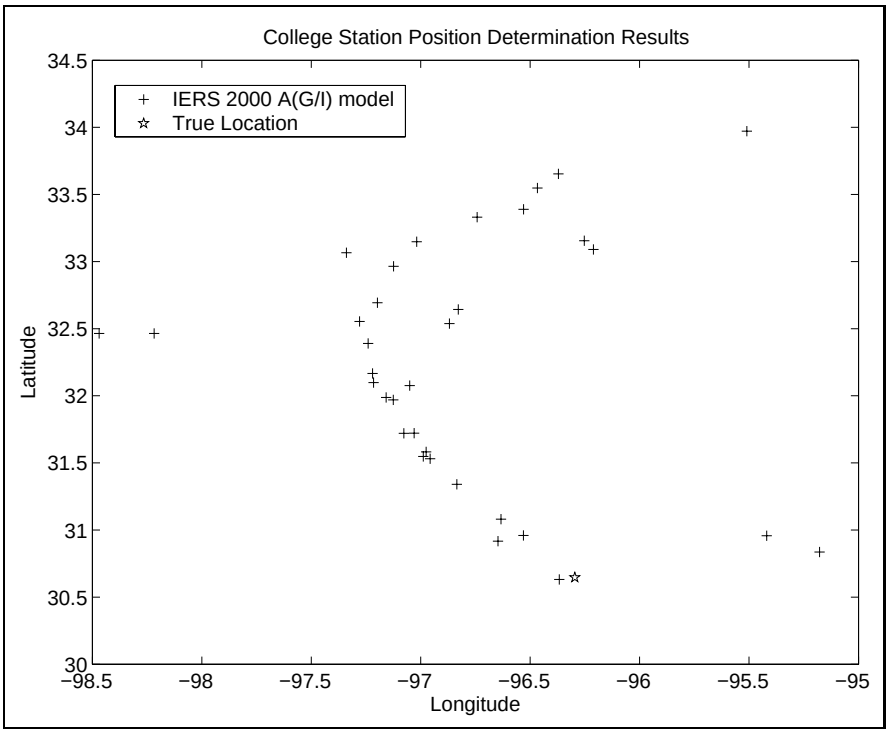

Fig. 27. College Station position determination results

The sensitivity of the $A^{B/I}$ matrix is made very clear by Fig. 27 where the average error of the position coordinates is 114.53 miles with a standard deviation of 73.78 miles. These results should not be considered a detraction from the positive results shown in Fig. 26, but rather a reminder of the highly sensitive nature of the position determination problem in general, and the attitude of the camera body with respect to the local reference frame in particular.

In conclusion, the CST performed relatively well for a proof-of-concept instru-

ment. The centroiding results for the ST-5C test images were not as good as a typical star tracker, but this can be attributed to the lack of imaging plane calibration. The position determination data analysis was significantly affected by the lack of inclinometer data, but the use of TheSky™ astronomy software allowed for the a thorough treatment of the data set. The sensitivities of the $A^{B/I}$ and $A^{G/I}$ matrices were evidenced the wide degree of variance in the position determination output.

CHAPTER VI

CONCLUSIONS

This research began with four primary objectives: to eliminate the zenith-orientation constraint, to design and build a proof-of-concept CST instrument, to conduct CST functionality experiments, and to conduct analyses of CST error sources. Each of these goals has been accomplished to varying degrees, but the overall research effort must be deemed a success. This chapter will briefly summarize the analytical, experimental, and theoretical efforts and results associated with each of the research goals. Those summaries will be followed with a short section regarding the future of the CST project.

A. Elimination of the Zenith-Orientation Constraint

This research has shown that camera operation in off-zenith alignments is feasible and desirable. If the CST were constrained to zenith-orientation operation, some system of moving parts would be required to align the camera's optical axis with the local zenith direction. The ability to operate in off-zenith alignments ensures that a CST instrument may be built with no moving parts, a distinct advantage in space hardware design.

The mathematics required to enable CST operation in off-zenith configurations was presented in Chapter II. The single-angle offset and dual-angle offset solutions were derived and applied to the general position determination problem. The effects of atmospheric aberration were included in the off-zenith mathematics.

The elimination of the zenith-orientation constraint does require the addition of a measurement sensor to determine the camera body's orientation with respect to the local reference frame. The primary sensor included in this research, a dual-axis

inclinometer, proved ineffective during the experimental test phase. However, the overall off-zenith capabilities of the CST were demonstrated by supplementing the CST test data with orientation information provided by astronomy software.

B. Proof-of-Concept CST Instrument Design and Fabrication

The instrument design and fabrication goal presented many interesting challenges, but in the end, a proof-of-concept CST instrument was built that generated experimental data. The primary challenges arose from the fact that many of the instrument design requirements were either unknown or established in real-time during the design process. Although an earlier completion of the CST error analysis would have yielded valuable insight into the selection of instrument components, the proof-of-concept instrument design is not drastically different than it would be if it were to be redesigned today. In addition to its ability to generate experimental data, the instrument design and fabrication goal was successful because the overall system was relatively simple to use during the instrument test program, and the total fabrication costs were kept extremely low due to the extensive use of COTS parts and the inelaborate camera body design.

The only major flaws in the proof-of-concept instrument are the ineffective dual-axis inclinometer and the modified ToUcam imaging sensor. These flaws are discussed in Chapter III. Chapter III also highlights the design improvements recommended for the next CST instrument. The suggested design improvements include a more effective means of aligning the optical axis direction, a better user interface, a fully-automated data management and algorithm processing capability, and a more accurate and sensitive inclinometer sensor.

C. CST Functionality Experiments

The CST test program included experimental tests in multiple geographic locations, at different times, and in various orientations with respect to the local zenith direction. In these regards, the test program met its research goal. The test program was also successful in that the processed experimental data clearly demonstrates the merit of the theoretical position determination concepts. Although it was impossible to isolate each of the test variables in a traditional scientific manner and the amount of experimental data was smaller than originally anticipated, the fact remains that the proof-of-concept instrument successfully collected enough experimental data to prove the theoretical concepts outlined in Chapter II.

D. CST Error Source Analysis

This research goal was met because the CST error source analyses were successfully completed. The results of those analyses are documented in Chapter IV. The analyses focused on the various factors that degrade the accuracy of the position determination results. The most sensitive source of CST error was determined to be the accuracy of the optical axis pointing direction. This error is due to a combination of inclinometer measurement accuracy and various mechanical tolerances. The other CST error sources that were discussed include the imaging sensor error and the image capture time error. In addition to the error analyses, potential solutions regarding each error source were discussed.

E. The Future of the CST Project

This research has clearly shown the efficacy of the theoretical position determination concepts and that the proof-of-concept CST instrument is an effective tool for the

demonstration of those concepts. When considering the various test data and results presented in this thesis, the reader should remember that the proof-of-concept CST instrument is simply a *proof-of-concept* instrument. This research was conducted on a part-time basis, with minimal design assistance, and with minimal cost. The potential for improvement is great. In order to improve the accuracy of the position determination output, the lessons learned through the course of this research should be implemented in the next embodiment of the CST concept.

By far, the most exciting aspect of the CST research is that the position determination concepts that have been demonstrated on Earth may one day be applied on the Moon and Mars. There are many developmental steps that must occur before that dream is realized, but the first step toward that goal has been taken. And like all first steps, it was an exciting one.

REFERENCES

[1] Samaan, M. A., Mortari, D., and Junkins, J. L., "Compass Star Tracker for GPS Applications," *AAS Guidance and Control Conference*, Breckenridge, CO, February 4-8, 2004, Paper No. AAS 04-007.

[2] Wahba, G., "A Least Squares Estimate of Satellite Attitude," *SIAM Review*, Vol. 7, No. 3, July 1965, pp. 409–410.

[3] Litwiller, D., "CCD vs. CMOS," *Photonics Spectra*, January 2001, Available at http://vfm.dalsa.com/shared/content/Photonics Spectra CCDvsCMOS Litwiller.pdf, [Accessed October 2005].

[4] Mortari, D., "Course Notes: AERO 689 Attitude Determination," Texas A&M University, College Station, TX, January-May 2005.

[5] Samaan, M. A., Mortari, D., and Junkins, J. L., "Non Dimensional Star Identification for Uncalibrated Star Cameras," *AAS/AIAA Space Flight Mechanics Meeting*, Ponce, Puerto Rico, February 9-13, 2003, Paper No. AAS 03-131.

[6] Mortari, D., Samaan, M. A., Bruccoleri, C., and Junkins, J. L., "The Pyramid Star Identification Technique," *Journal of The Institute of Navigation*, Vol. 51, No. 3, 2004, pp. 171–184.

[7] Vallado, D. A., *Foundations of Astrodynamics and Applications*, Kluwer Academic Publishers, El Segundo, California, 2nd ed., 2001, pp. 205–220.

[8] McCarthy, D. D. and Petit, G., "IERS Conventions (2003)," Technical Note 32, International Earth Rotation and Reference Systems Service, Frankfurt, Germany, 2004, pp. 33–53.

[9] "World Geodetic System 1984," STASYS Limited, Available at http://www.wgs84.com/, [Accessed October 2005].

[10] Chambers, S., "SC1 Modification," 2004, Available at http://www.pmdo.com /wintro.htm, [Accessed July 2005].

[11] Samaan, M. A., Griffith, T., Singla, P., and Junkins, J. L., "Autonomous On-Orbit Calibration of Star Trackers," *AAS/AIAA Space Flight Mechanics Meeting*, San Antonio, TX, January 27-30, 2002, Paper No. AAS 02-102.

[12] Mortari, D., "ESOQ-2 Single-Point Algorithm for Fast Optimal Spacecraft Attitude Determination," *Advances in the Astronautical Sciences*, Vol. 95, Pt. II, 1997, pp. 817–826.

[13] Høg, E., Fabricius, C., Makarov, V., Urban, S., Corbin, T., Wycoff, G., Bastian, U., Schwekendiek, P., and Wicenec, A., "The Tycho-2 Catalog of the 2.5 Million Brightest Stars," *Astronomy and Astrophysics*, Vol. 355, 2000, pp. L27–L30.

[14] Samaan, M. A., *Toward Faster and More Accurate Star Sensors Using Recursive Centroiding and Star Identification*, Ph.D. dissertation, Texas A&M University, College Station, TX, 2003.

APPENDIX A

COMPASS STAR TRACKER DRAWINGS

All information contained in the drawing files is the sole property of the Spacecraft Technology Center. Any reproduction in part or as a whole without the written permission of the Spacecraft Technology Center is prohibited. Accessing the drawings indicates acceptance of these terms.

The electrical and mechanical CST drawings may be accessed at:

http://handle.tamu.edu/

VITA

Michael John Swanzy earned his Bachelor of Science degree in mechanical engineering at Texas A&M University in College Station, Texas in 2001. After graduation, he held successive positions as a design engineer for the Boeing Company and a math teacher for the Fredericksburg Independent School District. He received a Master of Science degree in aerospace engineering from Texas A&M University in 2005. While attending graduate school, he has been employed by the Spacecraft Technology Center as a research and design engineer and undergraduate team mentor. He is currently engaged in the international affairs graduate school program at the George Bush School of Government and Public Affairs in College Station, Texas.

Mr. Swanzy may be contacted at the Spacecraft Technology Center, TAMU 3118, College Station, TX 77843-3118. His email address is mjs6343@yahoo.com.

This document was typeset in LaTeX by Michael Swanzy.